

DTIC FILE COPY

AFOSR-TR-88-1221

(2)

**RESEARCH ON SILICON, CARBON,
AND SILICON CARBIDE
HETEROSTRUCTURES**

DTIC
ELECTE
DEC 09 1988
S D
GZ VD

W. D. Partlow, W. J. Choyke, John T. Yates, Jr.,
L. E. Kline, R. R. Mitchell, Juai Ruan, J.V.R. Heberlein

Annual Report for the period
August 1, 1987 to August 1, 1988

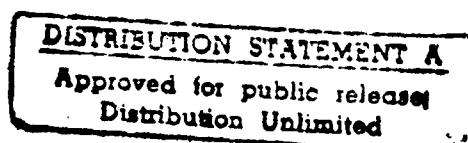
Contract No. F49620-87-C-0101

Air Force Office of Scientific Research
Bolling Air Force Base
Washington, DC 20332

Captain Kevin J. Malloy
Program Manager

Westinghouse R&D Center
General Order Number WGD 12021CE

September 26, 1988



AD-A202 866



Westinghouse R&D Center
1310 Beulah Road
Pittsburgh, Pennsylvania 15235

88 12 8 059

RESEARCH ON SILICON, CARBON, AND SILICON CARBIDE HETEROSTRUCTURES

W. D. Partlow, W. J. Choyke, John T. Yates, Jr.,
L. E. Kline, R. R. Mitchell, Juai Ruan, J.V.R. Heberlein

Annual Report for the period
August 1, 1987 to August 1, 1988

Contract No. F49620-87-C-0101

Air Force Office of Scientific Research
Bolling Air Force Base
Washington, DC 20332

Captain Kevin J. Malloy
Program Manager

Westinghouse R&D Center
General Order Number WGD 12021CE

September 26, 1988



Accession For	
NTIS CRA&I	<input checked="checked" type="checkbox"/>
DTIC TAB	<input type="checkbox"/>
Unannounced	<input type="checkbox"/>
Justification	
By	
Distribution /	
Availability Codes	
Dist	Avail and/or Special
A-1	



Westinghouse R&D Center
1310 Beulah Road
Pittsburgh, Pennsylvania 15235

SECURITY CLASSIFICATION OF THIS PAGE

REPORT DOCUMENTATION PAGE

Form Approved
OMB No. 0704-0188

1a. REPORT SECURITY CLASSIFICATION Unclassified			1b. RESTRICTIVE MARKINGS		
2a. SECURITY CLASSIFICATION AUTHORITY			3. DISTRIBUTION/AVAILABILITY OF REPORT Approved for public release; distribution unlimited.		
2b. DECLASSIFICATION/DOWNGRADING SCHEDULE			5. MONITORING ORGANIZATION REPORT NUMBER(S) AFOSR-TR, 88-1221		
4. PERFORMING ORGANIZATION REPORT NUMBER(S) 88-9531-HETRO-R1			7a. NAME OF MONITORING ORGANIZATION Air Force Office of Scientific Research		
6a. NAME OF PERFORMING ORGANIZATION Westinghouse R&D Center		6b. OFFICE SYMBOL (if applicable)	7b. ADDRESS (City, State, and ZIP Code) Bolling AFB, DC 20332		
6c. ADDRESS (City, State, and ZIP Code) 1310 Beulah Road Pittsburgh, PA 15235		7c. ADDRESS (City, State, and ZIP Code) Bolling AFB, DC 20332			
8a. NAME OF FUNDING/SPONSORING ORGANIZATION Air Force Office of Scientific Research		8b. OFFICE SYMBOL (if applicable) NE	9. PROCUREMENT INSTRUMENT IDENTIFICATION NUMBER F49620-87-C-0101		
8c. ADDRESS (City, State, and ZIP Code) Bolling AFB, DC 20332		10. SOURCE OF FUNDING NUMBERS			
		PROGRAM ELEMENT NO. 101102F	PROJECT NO. 2306	TASK NO. B1	WORK UNIT ACCESSION NO.
11. TITLE (Include Security Classification) Research on Silicon, Carbon, and Silicon Carbide Heterostructures					
12. PERSONAL AUTHOR(S) W. D. Partlow, W. J. Choyke, John T. Yates, Jr., L. E. Kline (see title page)					
13a. TYPE OF REPORT First Annual		13b. TIME COVERED FROM 8/1/87 TO 8/1/88		14. DATE OF REPORT (Year, Month, Day) 1988, September 26	
				15. PAGE COUNT 52	
16. SUPPLEMENTARY NOTATION					
17. COSATI CODES			18. SUBJECT TERMS (Continue on reverse if necessary and identify by block number)		
FIELD	GROUP	SUB-GROUP	PLASMAS, DEPOSITION, THIN FILMS, SILICON CARBIDE, DIAMOND, SURFACES, DESORPTION, CHARACTERIZATION, HETEROSTRUCTURES. (JF)		
19. ABSTRACT (Continue on reverse if necessary and identify by block number) The progress made during the first year of a three-year program to study heterostructures of Group IV materials is reported here. The equipment for the three experimental components of the program was assembled and characterized. These facilities include a remote plasma deposition reactor with extensive process diagnostics, an UHV apparatus for quantitative studies of the kinetics of adsorption/desorption of reactive species on atomically clean silicon surfaces, and an UHV, cryogenic cathodoluminescence spectroscopic facility. A model for the production, losses, and transport of metastable species in the remote reactor was completed. Experiments have begun to determine the reactive species present in the deposition process, the reaction of ethylene at silicon surfaces, and the cathodoluminescence of carbon in the diamond phase.					
20. DISTRIBUTION/AVAILABILITY OF ABSTRACT <input checked="" type="checkbox"/> UNCLASSIFIED/UNLIMITED <input type="checkbox"/> SAME AS RPT <input type="checkbox"/> DTIC USERS			21. ABSTRACT SECURITY CLASSIFICATION Unclassified		
22a. NAME OF RESPONSIBLE INDIVIDUAL D. H. H.			22b. TELEPHONE (Include Area Code) 202 761-4231		22c. OFFICE SYMBOL NE

CONTENTS

1.	PROGRAM OVERVIEW.....	1
2.	CHARACTERIZATION OF THE DEPOSITION PROCESS.....	3
3.	MODELING OF THE DEPOSITION PROCESS.....	4
4.	CHEMISTRY OF REACTIVE SPECIES AT SILICON SURFACES.....	5
5.	CATHODOLUMINESCENCE OF GROUP IV MATERIALS.....	6
6.	PUBLICATIONS AND INTERACTION ACTIVITIES.....	7
	APPENDIX I: CHARACTERIZATION OF THE DEPOSITION PROCESS.....	8
	APPENDIX II: MODELING OF ARGON DISCHARGE.....	21
	APPENDIX III: THE REACTION OF ETHYLENE WITH Si (100).....	32
	APPENDIX IV: CATHODOLUMINESCENCE EXPERIMENTS.....	46

RESEARCH ON SILICON, CARBON, AND SILICON CARBIDE HETEROSTRUCTURES

1. PROGRAM OVERVIEW

The program is a three-year effort to deposit thin films of group IV materials and heterostructures in a highly controlled and characterized deposition process and to gain an understanding of the process and of the deposited materials. The deposition process, remote plasma chemical vapor deposition, or RPCVD, uses a flowing afterglow of metastable rare gas atoms (in this case) to dissociate injected reactants such as methane or silane into desired deposition precursors. The process understanding is being obtained by carrying out extensive characterization experiments, such as direct measurement of metastable densities and deposition precursors, and by modeling the kinetics of the excitation, recombination, and reaction of the gases. Also a detailed study of the fundamental reactions at silicon surfaces of relevant deposition precursors, such as the methyl radical, is being carried out to provide basic insight into the deposition process. Besides the conventional techniques that will be used to characterize the deposited films, a special technique, cryogenic cathodoluminescence measurements in an ultrahigh vacuum apparatus, is being applied to this study.

The first year of the three-year program has been spent mainly on assembling and characterizing the experimental apparatus. The different groups involved in the program have been able to proceed beyond this to the stage of making experimental measurements relevant to the program's scientific objectives. The four main components of the program, and their respective technical leaders and locations are:

- a. Thin film deposition, process characterization, and conventional materials characterization: W. D. Partlow, Westinghouse R&D Center (Principal Investigator).
- b. Process modeling: Dr. L. E. Kline, Westinghouse R&D Center.
- c. Fundamental surface studies: Prof. John T. Yates Jr., Department of Chemistry, University of Pittsburgh.
- d. Cryogenic cathodoluminescence measurements:
Prof. W. J. Choyke, Department of Physics, University of Pittsburgh.

A technical overview of the approaches and progress of all of these aspects of the program will be presented in the next four sections. Details of the experimental and theoretical studies performed in these program components are reported in the appendices to this report. A final section describes the publication and interaction activities relevant to the program.

2. CHARACTERIZATION OF THE DEPOSITION PROCESS

The microwave-excited flowing afterglow of Ar that is required for activation of deposition reactions has been experimentally characterized. A description of these measurements is presented in detail in Appendix I. The densities of the metastable states of Ar in the 3P manifold were measured directly by excited state absorption of Ar resonance radiation and were compared to the theoretical calculations that will be described in Section 3. Besides the metastable species that we measured in the afterglow, we found significant populations of energy states, such as the 3P_1 , having lifetimes too short to be classified as metastable. Several such states were identified both by absorption and emission spectroscopy and are expected to have a major influence on deposition chemistry. We concluded that they are at least in part due to direct downstream excitation of Ar by charged species, since we were able to eliminate their downstream optical emission by inserting charged particle-collecting grids into the flow stream. Experiments are continuing to fully control and characterize the composition of the afterglow and to determine the influence of its composition on the properties of the deposited films.

3. MODELING OF THE DEPOSITION PROCESS

We have modeled the microwave-excited argon discharge that excites the flow gas for creation of metastables in the afterglow for the initiation of the deposition reactions. The operating point was calculated for stable argon discharges at the geometry and power densities characteristic of our experiments. This was done by balancing the production and losses of electrons in the plasma by solving the Boltzmann equation. This determined the field/gas density ratio, E/n , at which the discharge operates, and which determines the rate coefficients for the most important processes. The appropriate rate coefficients from the literature were used in a rate equation model to describe the plasma kinetics. The resulting predictions for densities of Ar metastables were compared to the experimental measurements. The predicted values have been higher than the measured values, and we are examining the model and critically evaluating the published data we used to explain the disagreement. One important quantity, the electron quenching rate for Ar metastables, varies by about a factor of three among four authors who reported it in the literature. We also are taking into consideration the influence of the high ionization fraction of these particular plasmas on the shape of the electron energy distribution. This may have a dramatic influence on the predicted metastable densities.

The model predicts a dependence of metastable production on power which reflects the operation of the plasma in several different regions having different important quenching behavior. Measured power density curves appear to reflect some of this structure.

These calculations are described in more detail in Appendix II of this report.

4. CHEMISTRY OF REACTIVE SPECIES AT SILICON SURFACES

Construction and testing of a UHV apparatus for study of the reactions of hydrocarbon species with Si surfaces has been completed. This apparatus has the following features:

- a. Sample mounting, heating, and ion bombardment capabilities needed for preparation and characterization of atomically clean surfaces,
- b. Absolutely calibrated molecular doser,
- c. Beam shutter for adsorption/desorption kinetics studies,
- d. Quadrupole mass spectrometer,
- e. Auger spectrometer.

A quantitative study of the reaction of ethylene with Si(100) surfaces has been carried out on this apparatus. The study, described in Appendix III, was successful in identifying a mobile precursor state for the adsorption of ethylene and determining the energetics for reaction and desorption of this molecule. Also, the saturation coverage and the decomposition of desorbed molecules were determined. A surface model to describe these data is being developed.

An azomethane source has been prepared. It will be used for the study of the reactions of methyl radicals with Si surfaces.

5. CATHODOLUMINESCENCE OF GROUP IV MATERIALS

The cathodoluminescence facility will make it possible to obtain characterization data highly relevant to the electronic properties of the materials. This facility is unique and takes advantage of developments in vacuum technology that make it possible and practical to make good cathodoluminescence measurements at low temperatures. The facility is now in operation, and cathodoluminescence spectra at temperatures as low as 60K have been obtained on natural diamond samples and on CVD diamond films that were deposited in our laboratory. Heat shields and temperature measurement techniques are presently being improved to permit measurements near 4.2K. Details of the facility are described in Appendix IV.

6. PUBLICATIONS AND INTERACTION ACTIVITIES

The publication activities are just beginning, as the experimental results become available on different program tasks. The experimental work on ethylene interactions at Si surfaces is being prepared for journal publication. A poster paper on the cathodoluminescence facility - "An Ultra High Vacuum-Liquid Helium Cathodoluminescence Monochromator for Large Band Gap (Diamond) Thin Film Analysis," W. J. Choyke - was presented at the Third Annual SDIO/IST-ONR Diamond Technology Initiative Symposium in July 1988 in Arlington, Virginia.

Several publications that are outgrowths of the program which preceded the present one - "Plasma Deposition of Silicon Carbide Films" - have appeared and will be mentioned because they are relevant to the program now in place. A comprehensive article on the carbon film deposition kinetics work that we concluded - "Electron and Chemical Kinetics in Methane RF Glow Discharge Deposition Plasmas," L. E. Kline and W. D. Partlow - is scheduled to appear in the Journal of Applied Physics on December 15, 1988. A collaboration with NASA workers on Silicon Carbide films that were developed on the program - "Grazing Incidence Reflectance of SiC Films Produced By Plasma-Assisted Chemical Vapor Deposition," Ritva A. M. Keski-Kuha, John F. Osantowski, Albert R. Toth, and William D. Partlow - was published in Applied Optics 27 No. 8, 1499 (April 1988). A paper describing the silicon carbide deposition kinetics - "Electron and Chemical Kinetics in Low Pressure RF Discharge Deposition of Amorphous Silicon-Carbide Thin Films," L. E. Kline and W. D. Partlow - has appeared in the Proceedings of the Eighth International Symposium on Plasma Chemistry, Tokyo, Japan, August 1987.

APPENDIX I

CHARACTERIZATION OF THE DEPOSITION PROCESS

I. Experimental Apparatus

The deposition reactor consists of a microwave-excited flow tube from which excited argon atoms dissociate reactants, such as methane for carbon-containing films or silane for silicon-containing films, and the reactive species thus produced are flowed over a sample susceptor. The reactor is shown schematically in Figure 1 in side view, which also shows how grids are placed in the flow stream to control charged species. The excitation source is a 0-1.5 kW microwave source at 2.455 GHz equipped with constant frequency power control and four-phase load impedance characterization. A four-stub tuner is used to match the microwave excitation into a 2.54 cm cylindrical plasma tube exciter, which has 8.5 cm cylindrical extensions to attenuate the microwave fields. The flow tube expands to 4.8 cm diameter immediately downstream of the plasma excitation unit. The process pumping is done with a mechanical pump-backed Roots blower that has a nominal pumping speed of 1000 liter/second. The assembled system with valves and downstream pressure controller in place delivers 411 liter/second pumping capacity. This will produce a plug flow velocity of about $2.3(10)^4$ cm/sec in the 4.8 cm flow tube. This is adequate for transporting rare gas metastables from the excitation region to the reaction zone without significant losses. The sample susceptor accepts several different heating and cooling modules and can provide temperatures from room temperature to 900°C. It is interchangeable with a differentially pumped mass spectrometer for sampling neutral and ionized species from the deposition gases.

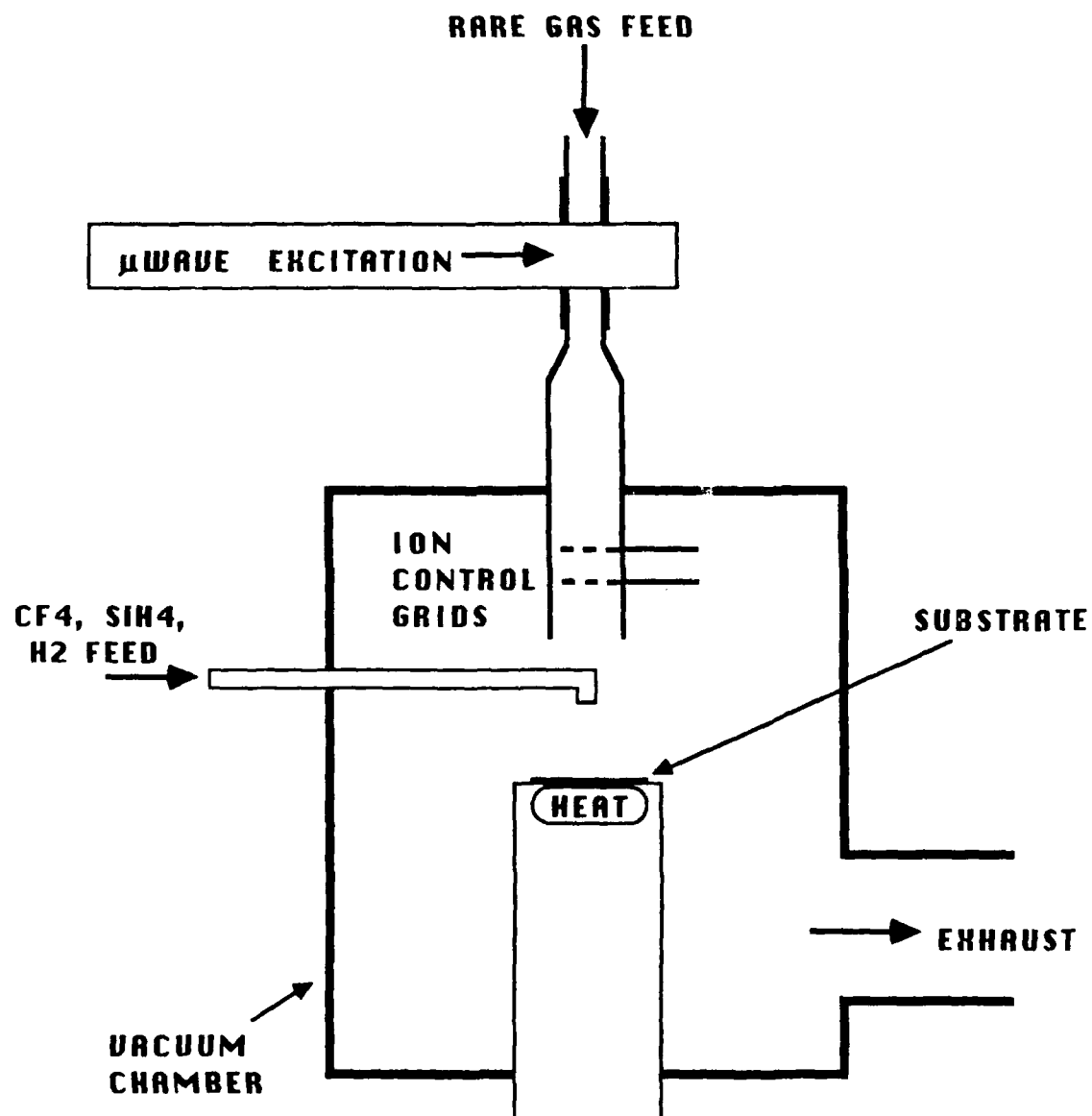


Figure 1. Schematic of the remote plasma CVD reactor.

The purpose of these characterization measurements is to obtain the information needed to gain an understanding of the production of reactive species that lead to deposition, and to control these species to change the properties of the deposited films. The first step is to determine which species from the excitation region reach the reaction zone. We are currently obtaining this information for argon flow gases by using two diagnostic techniques: optical absorption and emission spectroscopy. A top view schematic of the deposition reactor provided in Figure 2 shows how these diagnostics are arranged. The emission spectrometer consists of a 0.25 meter Jarrell Ash monochromator with computer control. A 0.3 meter McPherson monochromator is used for absorption of resonance emission lines from an Ar discharge tube. The light from the absorption source is chopped at 200 Hz, and synchronous detection provides discrimination from any light produced in the deposition reactor from the excitation plasma or from species that flow to the reaction zone. A beam splitter and filtered detector are used to monitor the output of the resonance radiation used for the absorption measurements so that some of the advantages of double-beam spectroscopy can be obtained.

A photograph is shown in Figure 3 of the deposition facility and its diagnostic equipment.

II. Optical Emission Measurements

Argon metastables in the 3P manifold located 11.5 to 12 eV above the ground state do not lead to visible emission, so the visible emission seen in the afterglow when no grids are used is an indication that other excited species are present. A photograph of the afterglow under typical operating conditions, presented in Figure 4, shows this emission clearly, and its visible emission spectrum is shown in

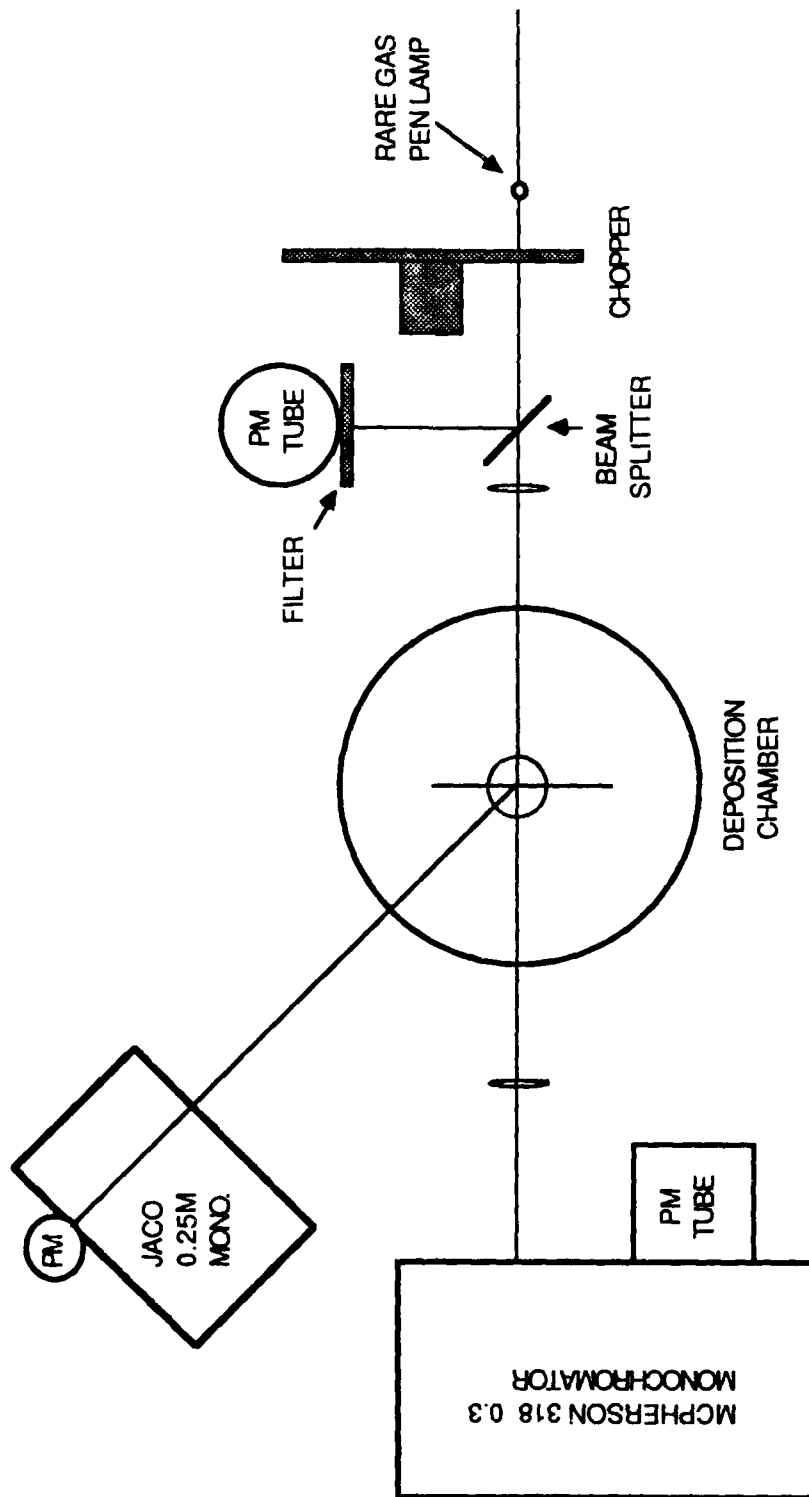


Figure 2. Schematic top view of the optical diagnostics on the RPCVD reactor.

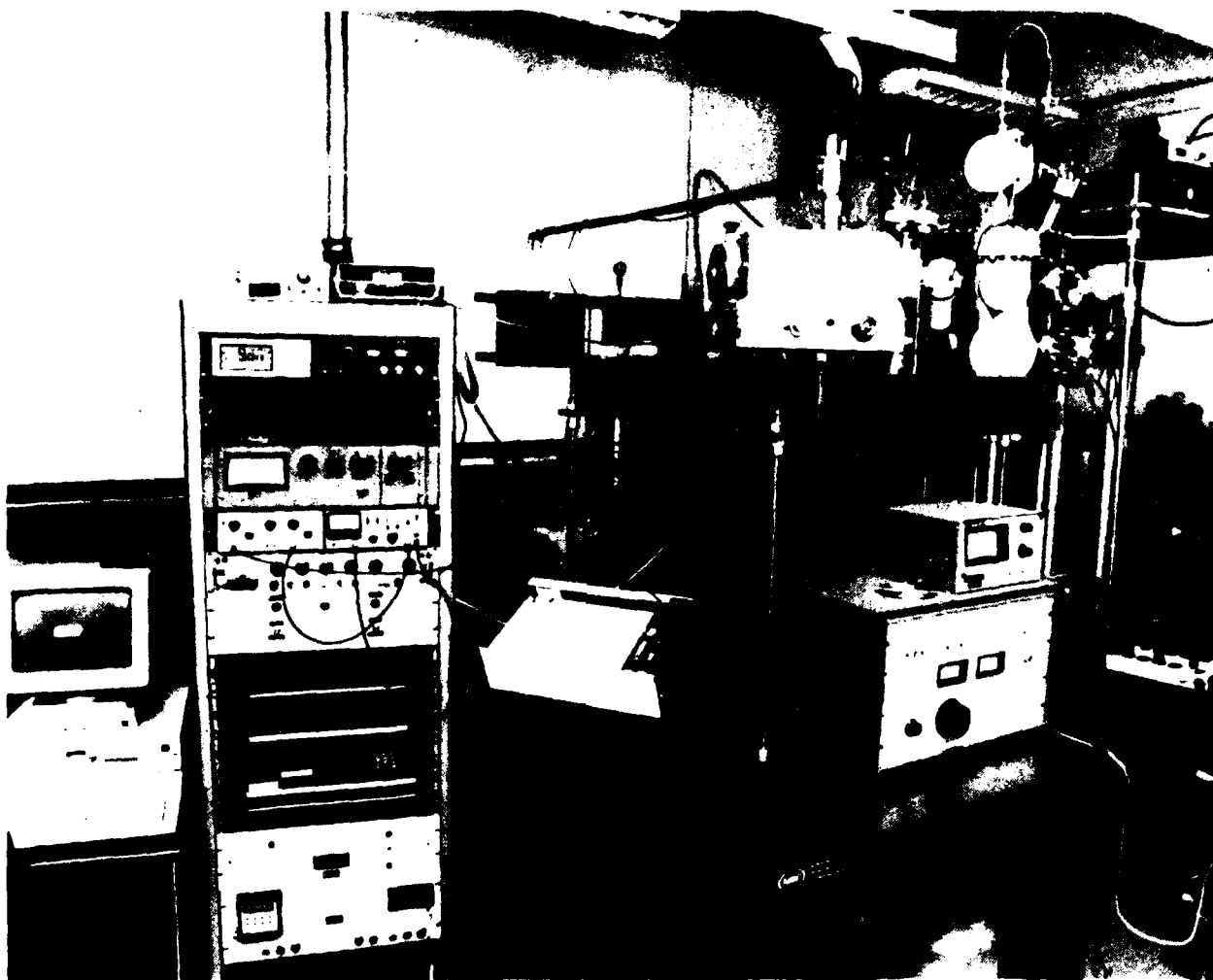


Figure 3. Remote plasma CVD experimental facility.

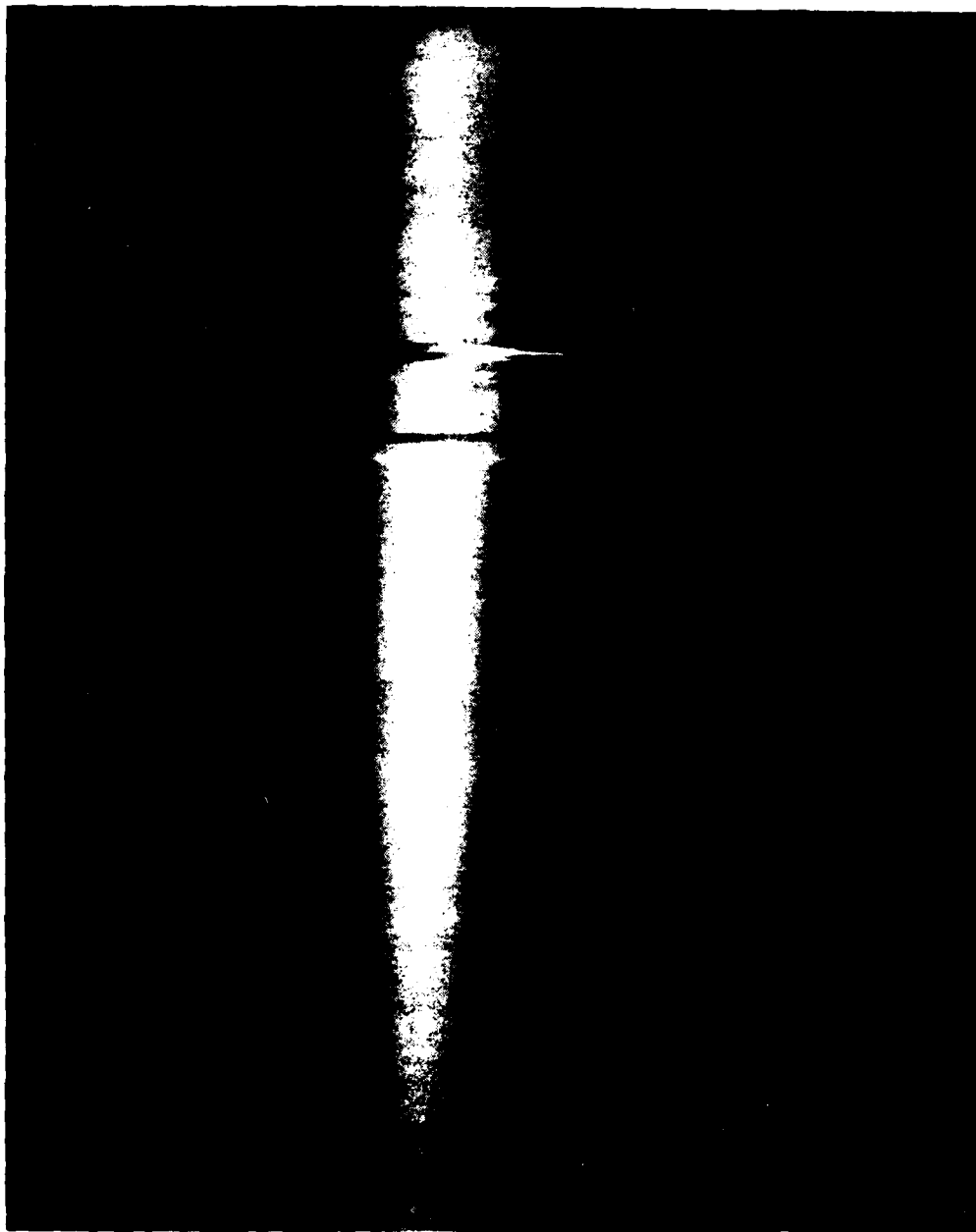


Figure 4. Photograph of flowing argon afterglow w. h no grids in the flow tube.

Figure 5. At low excitation powers, emission from the afterglow disappears when grounded grids are inserted into the flow stream, indicating that the emission is due to charged species directly exciting the gas in the afterglow region. Some visible afterglow is seen at higher powers, but there are indications that this is due to leakage around the grids. We have redesigned the grids to eliminate this leakage and plan to measure grid currents as a function of grid bias, and to correlate these measurements with non-metastable species detected downstream.

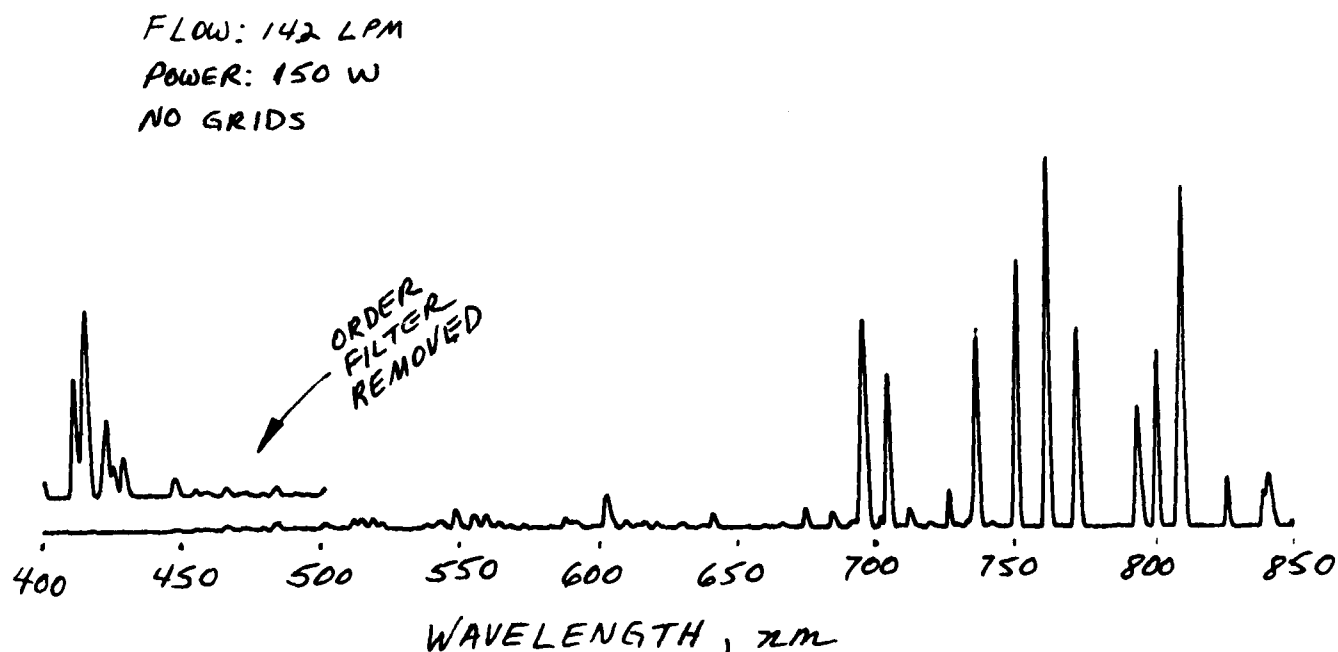


Figure 5. Spectrum of the argon flowing afterglow with no grids in flow tube.

III. Optical Absorption Measurements

Excited state absorption from the metastable 3P levels is easily detected by the absorption diagnostic. Absorbances of over 60% are measured at the highest powers at 811.5 nm, the strongest absorbing line from the 3P_2 state. An example of the raw absorbance data is shown in Figure 6, where it is plotted as a function of pressure. The density of the metastables can be obtained from this absorption data with a considerable effort of data analysis. The difficulty is due to the fact that the (Doppler) linewidth of the Ar lines used to measure the absorption is broader than the linewidth of the measured Ar absorption line, and these linewidths are not accurately characterized. They also depend upon temperature. The absorption does not obey the Beer-Lambert absorption law, absorbance values saturating at values below unity. We used a technique developed by Piper et al.,¹ which utilizes absorption measurements made with lines from the same state having different oscillator strengths. We also made measurements with different metastable densities. This provides an effective in-situ technique for determining the linewidth information that is required for determining densities. It basically consists of determining the kl values (absorption coefficient multiplied by absorption length) for several values of a , the ratio of source to sample linewidths. Sample density depends on:

$$kl/f,$$

where f is the oscillator strength of the transition. The same sample density should be predicted from measurement of different absorption lines from the same state. The value of a is used, which gives the most consistent density predictions for the same density and does this over a wide range of densities. The variation in density was obtained by varying the discharge power, and the resulting kl/f values as a function of power for four different a values are shown in Figure 7. An examination of the data shows that a values of 2.5 give the tightest patterns over the entire range of discharge powers. It is significant

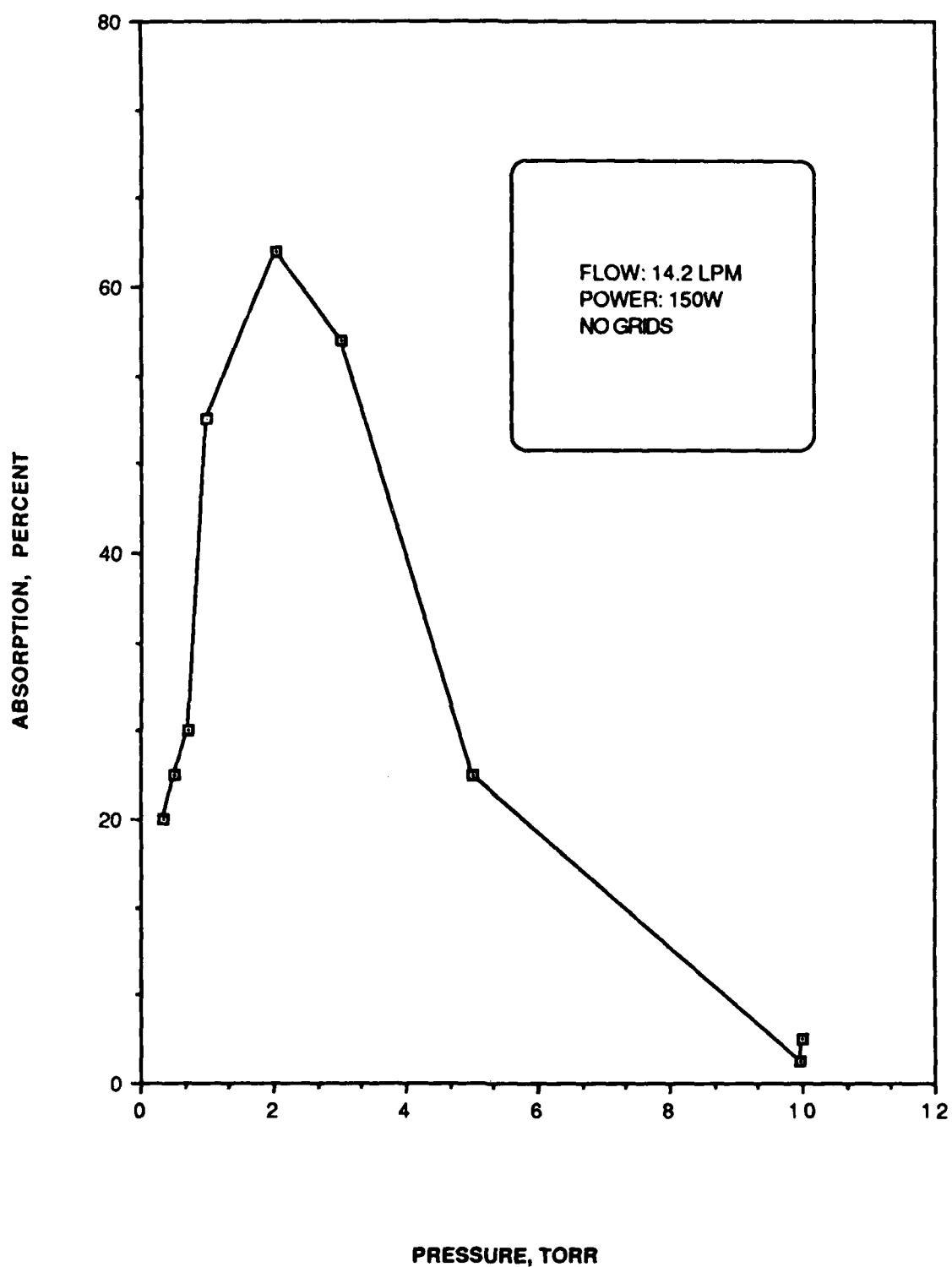


Figure 6. Absorption at 811.5 nm from the Ar 3P_2 state versus pressure.

that lower α values are not best at high powers, as would be expected if there were broadening of the afterglow lines due to heating from the discharge. An additional confirmation of our selection of α is obtained from Figure 8, where kl/f versus f is plotted for a single value of discharge power. Systematic departures from the ideal independence of kl/f on f are seen for α values above and below 2.5.

The densities determined by absorption spectroscopy of the 3P levels at 2 torr pressure (without grids) are plotted in Figure 9. The ratio of the 3P_2 to the 3P_0 densities are comparable to measurements of other workers.^{1,2} The significantly high density of the 3P_1 state, which has a lifetime of about 10 microseconds and is not metastable, gives confirmation to our earlier conclusion that there is direct excitation in the afterglow. The departure from linearity of the power dependencies of the metastable densities is outside the experimental error that we ascribe to our absorption measurements. The modeling work to be discussed in the next section predicts such nonlinear behavior.

IV. Future Plans

More experiments will be done to determine the nature of the downstream excitation and to achieve the ability to control it. As we mentioned, biased grid measurements are planned for this purpose. In addition, we plan to test our conclusions by measuring emission from methane and nitrogen, both of which are sensitive to the composition of the afterglow, as well as from silane. These measurements, in conjunction with the modeling, will put us in a position to relate the properties of films deposited from the afterglow to the state of the afterglow excitation.

V. References

1. L. G. Piper, J. E. Velazco, and D. W. Setser, J. Chem. Phys. 59(6), 3323 (1973).
2. John Balamuta, Michael F. Golde, and Yueh-Se Ho, J. Chem. Phys. 79(6), 2822 (1983).

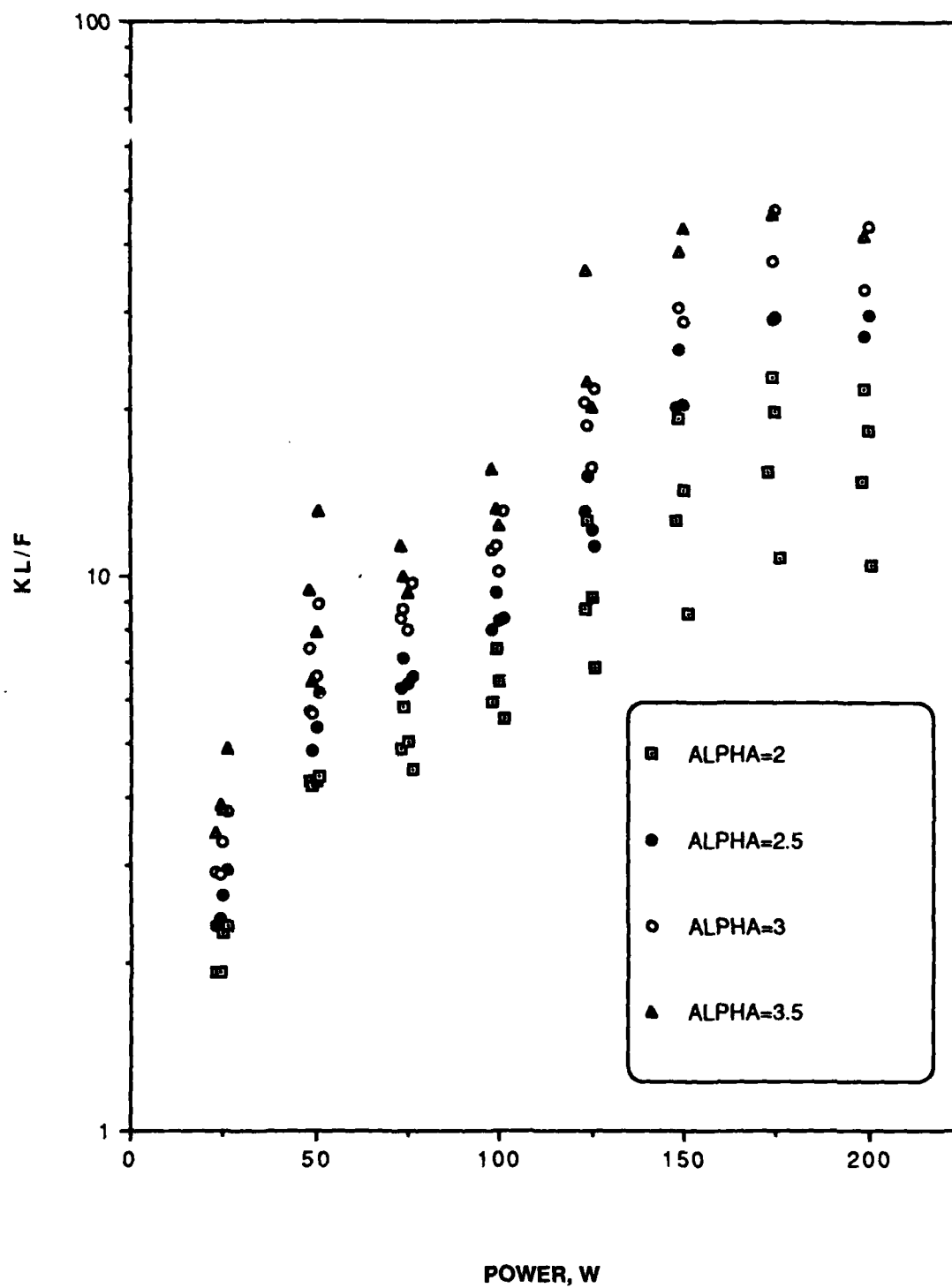


Figure 7. Plots of kl/f , proportional to density, for several values of α at different plasma powers.

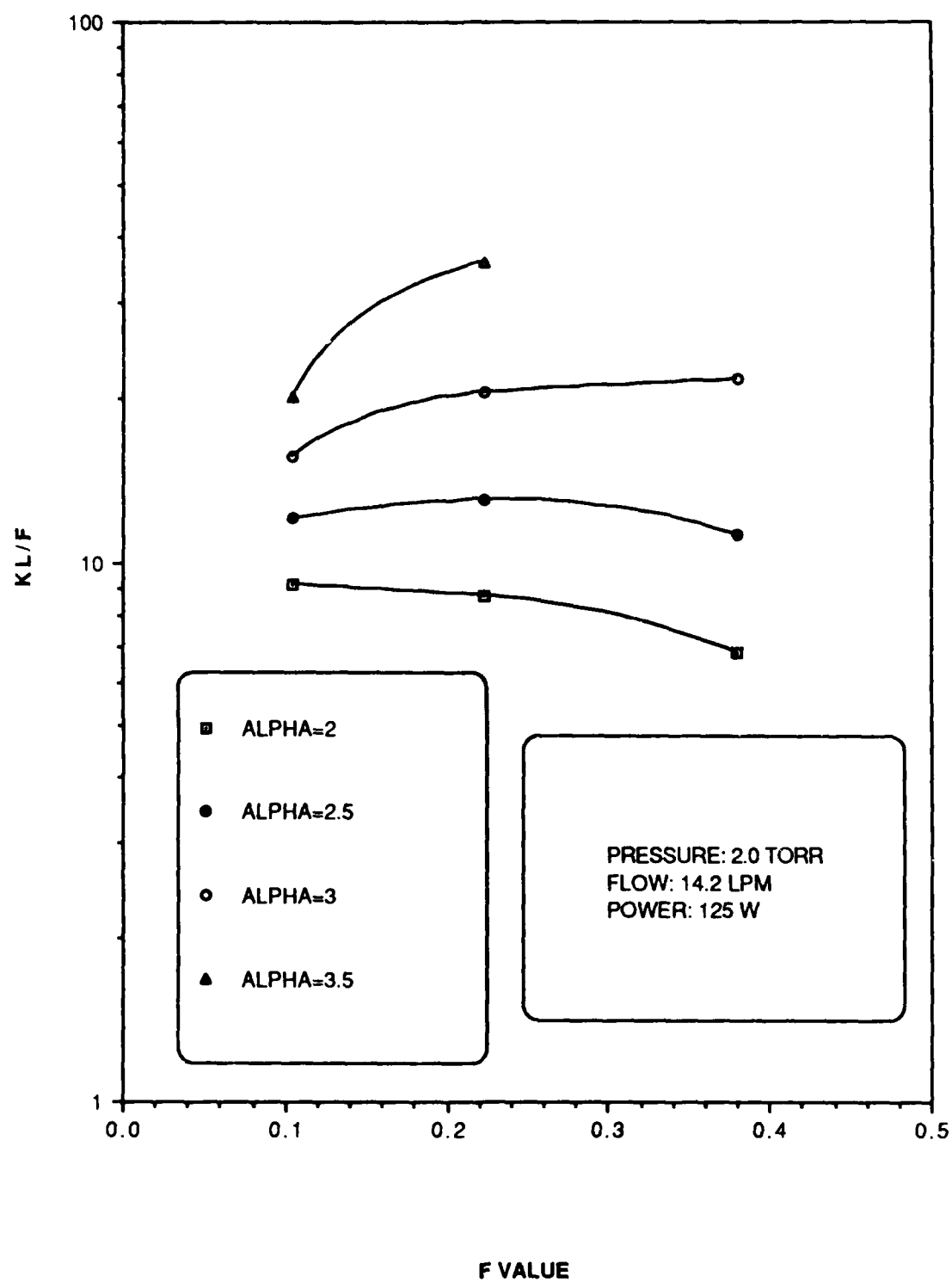


Figure 8. Plots of kl/f versus f for several values of α at a single discharge power.

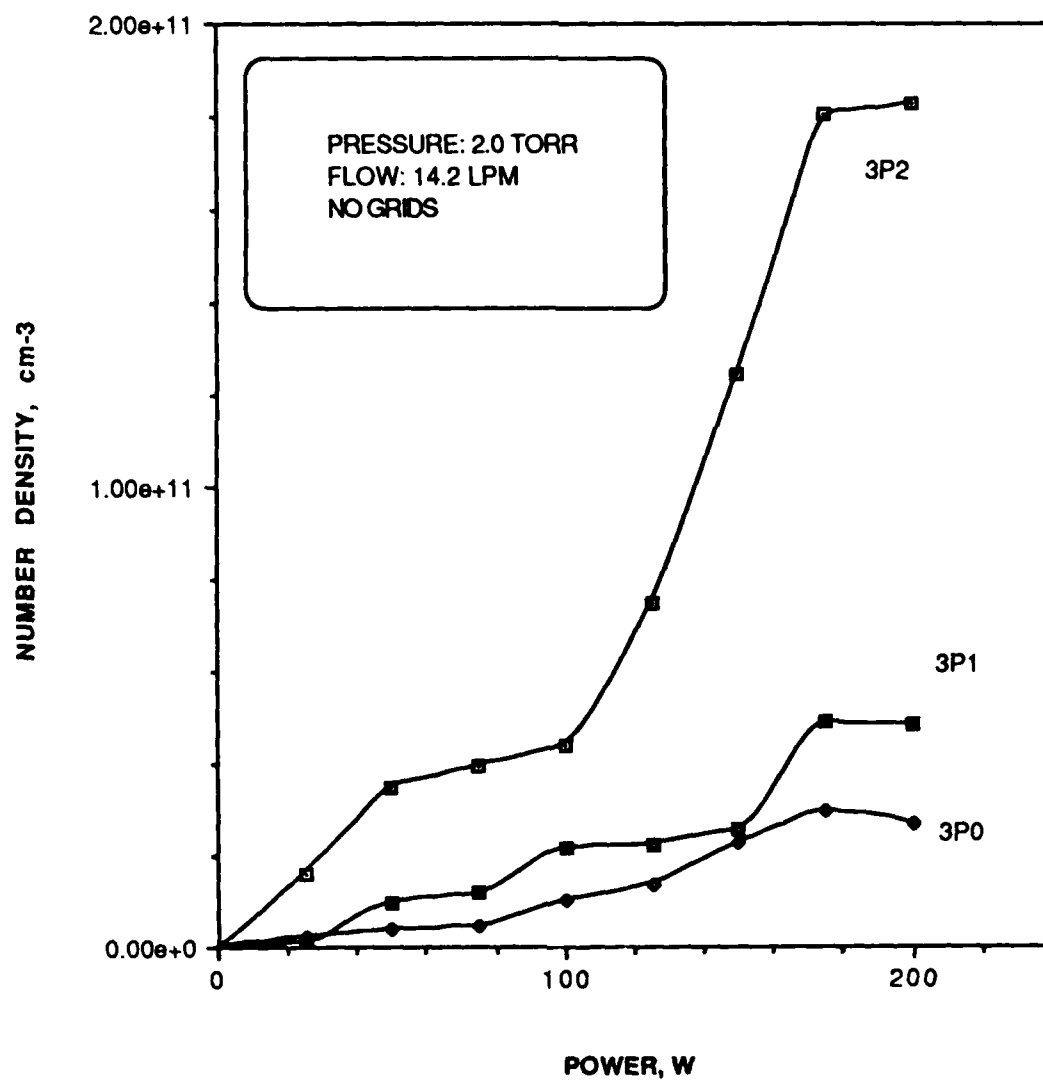


Figure 9. Measured values of excited state densities for the metastable $3P_2$ and $3P_0$, and the non-metastable $3P_1$.

APPENDIX II

MODELING OF ARGON DISCHARGE

Determination of Operating Point

The first step in modeling the argon microwave discharge is the determination of its operating point. This means finding the value of the ratio of the electric field to the gas density, E/N , at which the discharge operates. Let $(E/N)_G$ denote this value of E/N . Finding $(E/N)_G$ is of critical importance because it determines the rate coefficients for many important processes, such as the creation of metastable states of argon.

The discharge will operate at a steady state such that the production and loss processes for electrons are in balance. The only important production process is electron impact ionization of ground state argon atoms. Two-step ionization -- that is, electron impact ionization of argon metastables -- should not be important for expected metastable concentrations. At the anticipated operating pressures of a few Torr or less, the dominant electron loss process should be ambipolar diffusion to the walls of the discharge tube. Volume recombination and free electron diffusion are not significant. Such diffusion-dominated discharges are discussed, for example, by Cherrington.¹ In a steady-state, diffusion-dominated discharge, the electron conservation equation is

$$dn_e/dt = 0 = k_i n_e N - D_a n_e / \Lambda^2,$$

where n_e is electron density, k_i is the rate coefficient for electron impact ionization, N is the argon atom density, D_a is the ambipolar

diffusion coefficient, and $\Lambda = (\text{tube radius})/2.405$ is the characteristic ambipolar diffusion length. Thus, in steady-state the ionization rate per electron, ν_i , is given by

$$\nu_i = k_i N = D_a / \Lambda^2.$$

The two quantities to be determined as a function of E/N are k_i and D_a . k_i is found in a straightforward way by solving the Boltzmann equation. D_a is given¹ by:

$$D_a = \frac{D_e \mu_+ + D_+ \mu_e}{\mu_e + \mu_+}.$$

In discharges such as this where the electrons are strongly heated, it is true that $D_e \gg D_+$ and $\mu_e \gg \mu_+$. Thus, we have approximately

$$D_a = (D/\mu)_e \mu_+ + D_+.$$

Using a literature² value for μ_+ , we have

$$D_a p = (D/\mu_e) (1200) \text{ cm}^2 \text{ Torr/s}$$

for argon, where p is pressure in Torr.

Plots of ν_i and D_a/Λ^2 versus E/N are shown for 0.3 Torr and 2.0 Torr in Figures 1 and 2, respectively. The predicted $(E/N)_G$ for these two pressures are 60 Td and 28 Td, where $1 \text{ Td} = 1 \times 10^{-17} \text{ V cm}^2$.

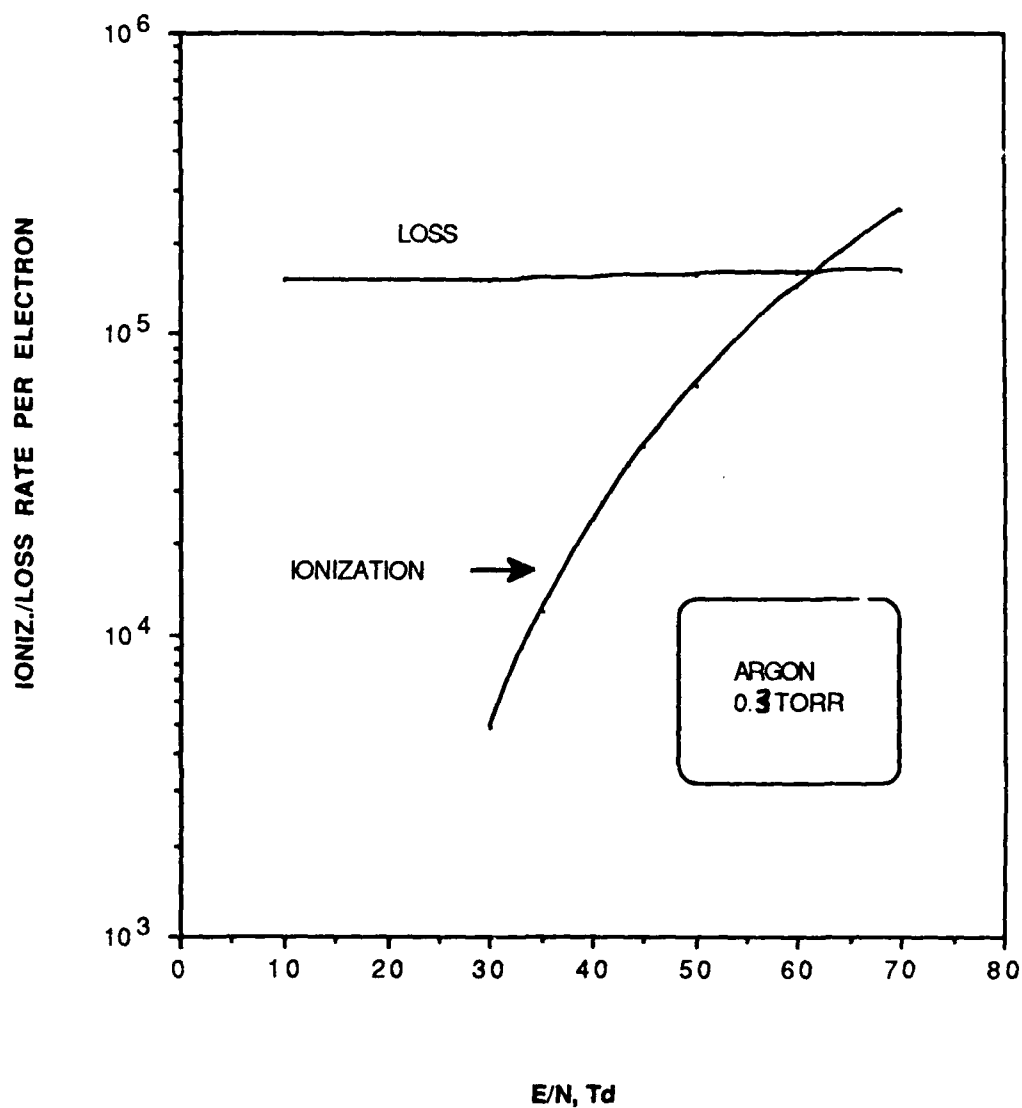


Figure 1. Ionization rate and diffusion loss rate versus E/N for argon in a cylindrical tube of 1.1 cm radius at a pressure of 0.3 Torr. The intersection of the curves is the predicted operating point of the discharge.

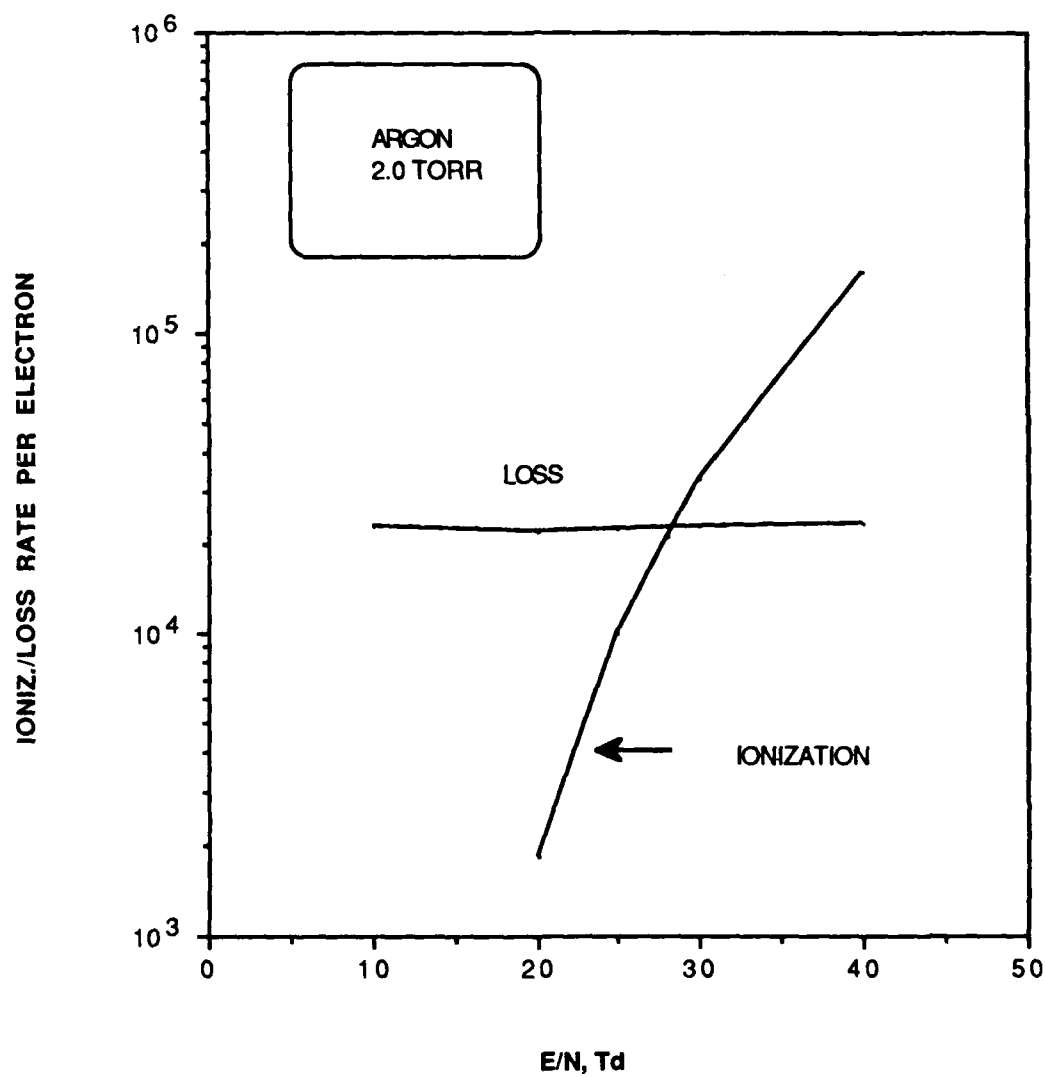


Figure 2. Ionization rate and diffusion loss rate versus E/N for argon in a cylindrical tube of 1.1 cm radius at a pressure of 2.0 Torr. The intersection of the curves is the predicted operating point of the discharge.

Solutions of the Boltzmann Equation

The cross sections used for the 4p states of argon are those of Tachibana.³ There are four 4p states, two of which are metastable. The metastable states are the 3P_2 and 3P_0 states at 11.55 eV and 11.72 eV. The two resonant 4p states are the 3P_1 at 11.62 eV and the 1P_1 at 11.83 eV. The other two cross sections found by Tachibana are for lumped states: the higher lying optically forbidden (mostly p) states and the higher lying optically allowed s and d states. The ionization cross section is that of Rapp and Englander-Golden.⁴

The 4p states, in addition to population through direct excitation, are also populated by cascading from the higher forbidden states. From measurements and Boltzmann calculations, Tachibana concludes that 39% of the total excitation of the higher forbidden states cascade to 3P_2 , while only 7% cascades to 3P_0 . The remainder of these states cascades to the resonant 3P_1 and 1P_1 states.

We have performed Boltzmann equation solutions for argon using the cross sections of Tachibana. We have determined excitation rate coefficients in cm^3/s for 0.3 Torr and 2.0 Torr as follows:

	<u>0.3 Torr (60 Td)</u>	<u>2.0 Torr (28 Td)</u>
3P_2	5.40(-11)	1.19(-11)
3P_1	5.59(-11)	1.63(-11)
3P_0	1.02(-11)	2.26(-12)
1P_1	8.63(-11)	2.29(-11)

Equation Discharge Model

The argon discharge has been modeled using a rate equation computer code developed by Lacina.⁵ The processes included in the model are shown in Table 1 along with their reaction rates. Processes 1-4 are electron impact excitation of the two metastable and two resonant 4p states. The rates for these are given above. Processes 5 and 6 are electronic quenching of the metastables. Quenching rates have been given by four authors and vary by about a factor of three. The rates adopted here are those of Bochkova and Sukiasyan⁶ for the 3P_0 state ($7 \times 10^{-7} \text{ cm}^3/\text{s}$) and Gerasimov and Petrov⁷ for the 3P_2 state ($4.5 \times 10^7 \text{ cm}^3/\text{s}$).

Reaction 7 is ionization with the rate from our Boltzmann calculations. Reactions 8 and 9 are two- and three-body quenching of metastables, which are included although they have not had a significant effect on any of the calculations thus far. The rates are taken from Kolts and Setser.⁸ Reactions 10 and 11 correspond to spontaneous radiation from the resonant states. The rates include the effect of radiation trapping and are estimates from Scheller et al. Reaction 12 represents the loss of positive ions due to ambipolar diffusion to the tube wall. It is treated as a volumetric loss with a rate determined by the discharge operating point.

The electron density is held fixed at a value chosen to match the expected discharge power density

$$E j = (E/N) N n_e e W .$$

Here e is the electronic charge and W is the electron drift velocity. E/N and W are determined by the discharge operating point through pressure and tube radius. Thus, according to the model, only n_e changes to correspond to varying experimental discharge power density.

Table 1. Summary of reactions used in the rate equation model for the argon discharge. The reactions are input in the form shown into the computer model, which forms a set of rate equations from the reactions. Rate coefficients are given for each reaction.

i	reaction(i)	kf(i)	kr(i)	references or comments
1	e + ar => ar(m) + e	1.1900e-11		Tachibana xsect, Fig book p. 30
2	e + ar => ar(m2) + e	2.2600e-12		Tachibana xsect, Fig book p. 30
3	e + ar => ar(r) + e	1.6300e-11		Tachibana xsect, Fig book p. 30
4	e + ar => ar(r2) + e	2.2900e-11		Tachibana xsect, Fig book p. 30
5	e + ar(m) => ar(r) + e	4.5000e-07	4.5000e-07	Gerasimov & Petrov
6	e + ar(m2) => ar(r2) + e	7.0000e-07	7.0000e-07	Bochkova & Sukiasyan
7	e + ar => ar(p) + e	3.1900e-13		Tachibana xsect, Fig book p. 28
8	ar + ar(m) => ar + ar	2.1000e-15	x e(-e/kt)	2-body quench
9	ar + ar(m) + m => ar + ar + m	1.1000e-32		3-body quench
10	ar(r) => ar	1.0000e+05		Scheller et al estimate
11	ar(r2) => ar	1.0000e+05		Scheller et al estimate
12	ar(p) => ar	2.2500e+04		Ambipolar diffusion, Fig book, p. 29

Note: Reactions no. 7 and no. 12 appear charge-unbalanced because of a formatting convention.

We simulated experimental conditions of 2.0 Torr and a power density of about 2 watts/cm³, corresponding to an electron density of 2.5×10^{11} cm⁻³. The resulting steady-state densities are shown in Table 2. The ³P₂ density of 6.45×10^{12} cm⁻³ is about 40 times higher than the measured value. Figure 3 shows the ³P₂ density as a function of time for the first 500 microseconds of discharge operation. In gas flowing at 250 m/s, this corresponds to a flow distance of 12.5 cm so the metastable density attains its full value in about 2 cm.

Table 2. Predicted steady-state species densities of an argon discharge with a pressure of 2 Torr and electron density of 2.5×10^{11} cm⁻³. The ar(m) and ar(m2) species are the ³P₂ and ³P₀ metastable states, while the ar(r) and ar(r2) are the resonant states and ar(p) is the positive ion. Excitation energy, rate of population change, and time constant are also given for each state.

time t = 5.000E-04 sec					
population densities and rates of change					
i	species name	e(i), (ev)	n(i) (cm-3)	dn(i)/dt (cm-3/sec)	tau(i) 1.0E-06 sec
1	rad	0.00	0.000E+00	0.000E+00	
2	e(-)	0.00	2.500E+11	0.000E+00	
3	ar	0.00	6.681E+16	2.211E+13	3.02E+09
4	ar(m)	11.55	6.454E+12	-8.151E+12	7.92E+05
5	ar(m2)	11.62	4.418E+12	-2.843E+12	1.55E+06
6	ar(r)	11.71	4.698E+12	-5.869E+12	8.00E+05
7	ar(r2)	11.83	4.203E+12	-2.147E+12	1.96E+06
8	ar(p)	15.80	2.369E+11	-3.102E+12	7.64E+04
total gas density			6.683E+16		
			integration step size =	69.269	
			order of integration =	4	

Dependence of Metastable Production on Power Density

The only significant process for metastable destruction is electron quenching, which produces a resonant state that can then radiate to the ground state. The estimated effective lifetime of the resonant states is 10 microseconds due to radiation trapping. This radiative lifetime competes with a lifetime due to electron impact of the resonant state that produces the metastable state. The rate for this process is given by

$$\nu_Q = k_Q n_e$$

where k_Q is the rate coefficient. Thus, for sufficiently high electron density, this process can dominate radiative decay and electron quenching is defeated. But in the other limit of low electron density, all quenched metastables are permanently lost because of radiative decay. In this case, the ratio of metastable to ground state densities is given by

$$[Ar^*]/[Ar] = k_* / k_Q$$

where k_* is the rate coefficient for 3P_2 production (reaction 1) and k_Q is the rate coefficient for 3P_2 quenching (the forward rate for reaction 5). Using the rate coefficients from Table 1, the fractional metastable density is 2.64×10^{-5} . For a pressure of 2 Torr this gives a predicted metastable density of $1.77 \times 10^{12} \text{ cm}^{-3}$ in the limit of low electron density.

For the case shown in Table 2 and Figure 3, the rate for electron impact de-excitation ($1.13 \times 10^5 \text{ s}^{-1}$) is nearly equal to the rate for radiation (10^5 s^{-1}). In this case the 3P_2 density is about four times the low n_e value. Increasing the electron density by a factor of four to 10^{12}

cm^{-3} increases the $^3\text{P}_2$ density by a factor of 3.2. A further order of magnitude increase results in the $^3\text{P}_2$ density rising by a factor of 9.2. Thus, the model predicts three regions:

- 1) For low electron density, metastable density is independent of electron density (power density).
- 2) For "intermediate" electron density, i.e., where the radiative and collisional depopulation of the resonant $^3\text{P}_1$ and $^1\text{P}_1$ states are comparable, there is a transition region where metastable density increases sublinearly with electron density.
- 3) For high electron density the metastable density increases linearly with electron density.

References

1. B. E. Cherrington, Gaseous Electronics and Gas Lasers, Pergamon Press (1979).
2. M. A. Biondi and L. M. Chanin, Phys. Rev. 94, 910 (1954).
3. K. Tachibana, Phys. Rev. A 34, 1007 (1986).
4. D. Rapp and P. Englander-Golden, J. Chem. Phys. 43, 1464 (1965).
5. W. B. Lacina, Final Technical Report, ONR Contract N00014-78-C-0499 (1979).
6. O. P. Bochkova and E. A. Sukiasyan, Zh. Prikl. Spek. 23, 801 (1975).
7. G. N. Gerasimov and S. Ya. Petrov, Opt. Spectrosc. 43, 7 (1977).
8. J. H. Kolts and D. W. Setser, J. Chem. Phys. 68, 4848 (1978).

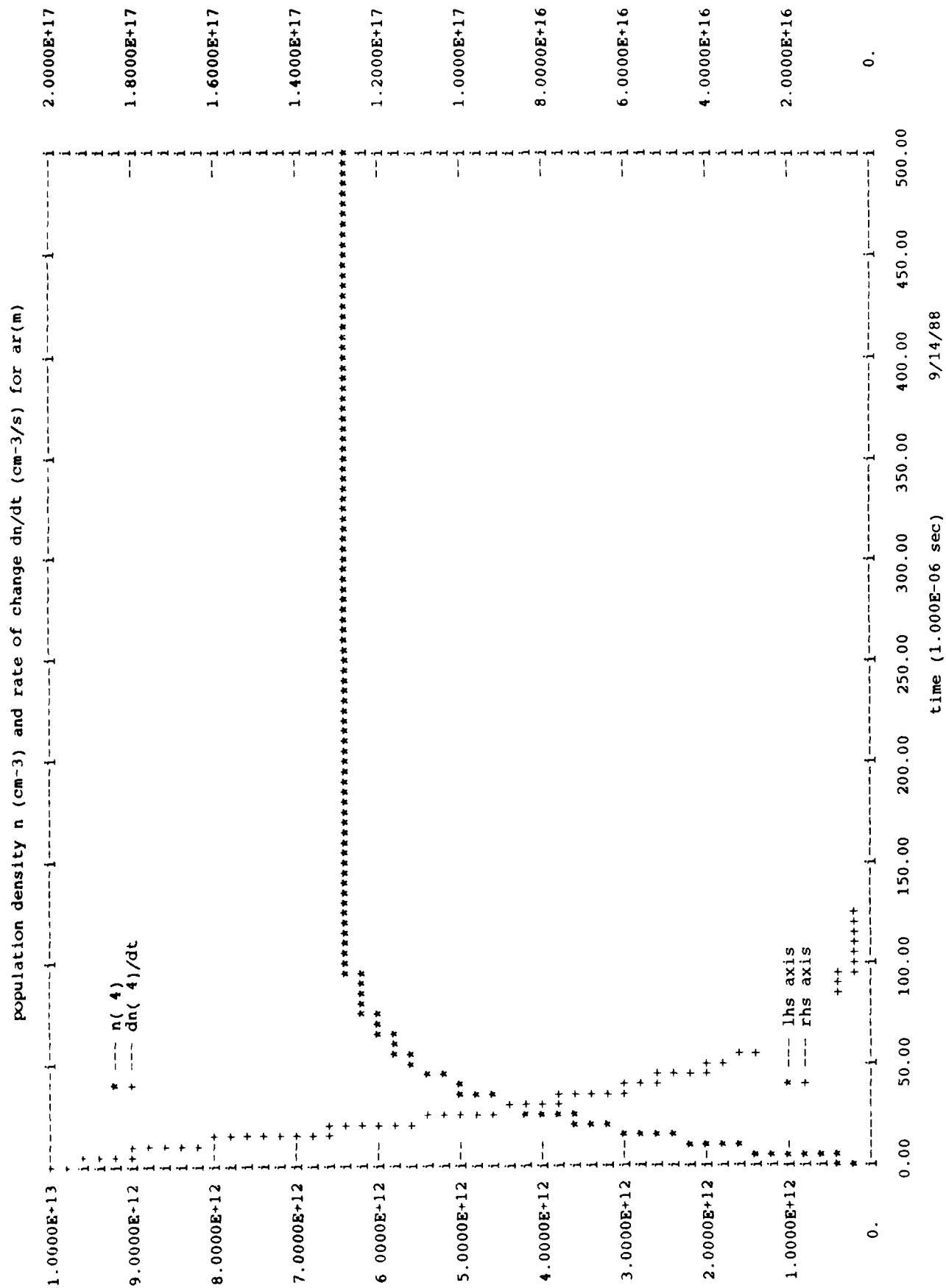


Figure 3. Predicted spatial behavior of the argon metastable density (***) and its time derivative (+++). The horizontal axis, which is labelled "time" and goes to 500 microseconds, corresponds to a total distance of 12.5 cm at the flow velocity of 250 m/s.

APPENDIX III

THE REACTION OF ETHYLENE WITH Si (100)

I. INTRODUCTION

Understanding the interaction of simple hydrocarbon molecules with silicon single crystal surfaces is of importance in determining the mechanism of formation of silicon carbide films on Si. The interaction of hydrocarbons with the dangling bonds at the Si surface represents the very first step in the silicon carbide thin film formation process. We have employed surface kinetic and surface spectroscopic methods to study the details of adsorption, thermal decomposition and reaction of the simplest olefin, ethylene, on the Si(100) surface.

It has previously been shown in our laboratory [1] and elsewhere [2] that the carbon-carbon double bond is an active center for reaction with atomically clean Si surfaces. Comparison experiments involving alkane and olefin molecules clearly show that at 120 K only the olefins react efficiently with the Si dangling bonds on Si(100) [3].

II. THE Si(100) SURFACE

It is well known that the Si(100) surface consists of rows of Si-Si dimers exhibiting a (2 x 1) lattice structure [4]. Each of the Si atoms in a dimer species contains an upward-directed Si dangling bond which can act as a reactive center for the adsorption of olefin molecules. A diagram of the Si dimer sites on Si(100) is shown in figure 1.

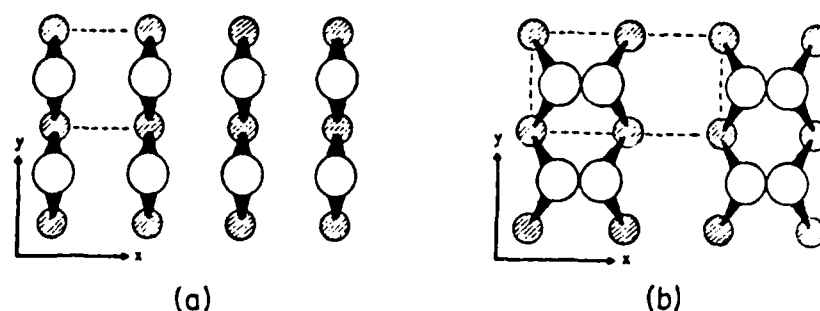


Figure 1. Ideal Si(100)(2x1) surface. The open and hatched circles represent the atoms in the topmost and second layers, respectively. (a) Unreconstructed surface. (b) Reconstructed surface containing Si-Si dimer species [5]. There are 3.4×10^{14} Si dimers/cm².

III. EXPERIMENTAL METHODS

A. Preparation of the Si(100) Surface

The Si(100) crystal (10 ohm-cm, B doped) is held between W heating support wires using Ta sheet spring clamps which grip the crystal internally in slots cut along the edges of the rectangular crystal [6]. In addition, a W/5%Re:W/26%Re thermocouple junction is contained inside a third slot in the crystal edge. This arrangement permits ohmic heating of the crystal for cleaning as well as for temperature programmed desorption spectroscopy measurements [6,7]. The crystal is ion bombarded with Ar⁺ (2k eV; 2.5 μ A/cm²; 1800 seconds) for initial cleaning and is then heated to 1190 K to remove the last traces of surface carbon and oxygen as measured by Auger spectroscopy. Care must be taken not to heat the crystal to temperatures above 1350 K in order to avoid irreversible damage to the crystal as observed by STM measurements [8]. Following cleaning, the crystal is cooled to about 100 K for adsorption studies.

B. Use of a Calibrated Directed Beam Doser for Adsorption

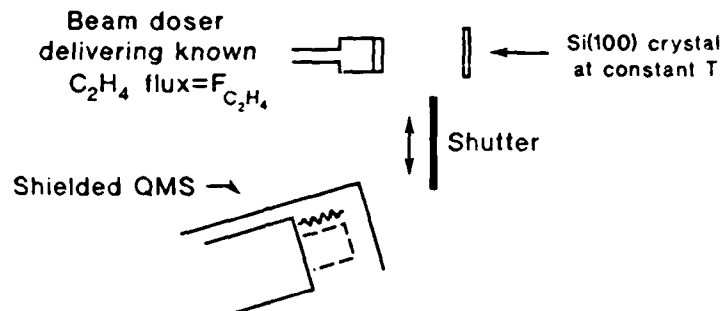
Fundamental insight into the stoichiometry of adsorption on single crystal surfaces may be made by employing quantitative adsorption measurements. This may be achieved through the use of a directed beam doser of our own design [6] which permits the establishment of an absolute known flux of adsorbate molecules which impinge on the single crystal surface. Through the use of a mass spectrometer for the detection of the reflected flux of molecules, it is possible to determine both the absolute coverage and the absolute reaction probability of the impinging molecules with the surface. The angular distribution of the gas from dosers of this design has been carefully investigated [9].

C. Apparatus for Adsorption-Desorption Kinetic Studies

Figure 2 shows a schematic diagram of the apparatus which has just been built for the study of hydrocarbon molecule adsorption on Si(100). It consists of a beam doser which delivers a known flux, $F_{C_2H_4}$, of ethylene to the crystal. The apparatus is equipped with a shielded quadrupole mass spectrometer which is arranged to receive only a random flux of gas which is either not adsorbed by the crystal or which misses the crystal and rebounds from the walls of the pumped ultrahigh vacuum chamber. A shutter may be rapidly moved into the C_2H_4 beam to protect the crystal from direct adsorption from the beam. The lower portion of figure 2 shows a schematic experiment in which adsorption by the Si(100) crystal is monitored by the mass spectrometer. A background level of C_2H_4 is initially present in the apparatus; the beam doser is turned on to admit C_2H_4 with the shutter in place to intercept the direct beam, and after a short time, a stable pressure of C_2H_4 is observed by the mass spectrometer due to reflection of all C_2H_4 gas from the back of the shutter. At this point, the shutter is removed and the C_2H_4 signal sharply decreases due to adsorption by the Si(100) crystal. The region of constant $P_{C_2H_4}$ is due to an adsorption process which occurs with a constant sticking coefficient equal to unity; following this region, the sticking coefficient drops as a slower adsorption process occurs, and the measured $P_{C_2H_4}$ signal rises asymptotically to the limit shown by the dashed line. At this point the rate of adsorption has dropped to near zero; placing the shutter in or out has no effect on the measured pressure of ethylene, since both the crystal and the shutter reflect 100% of the impinging C_2H_4 .

Kinetics of Adsorption of C_2H_4 by Si(100)

Schematic Apparatus



Schematic Experiment

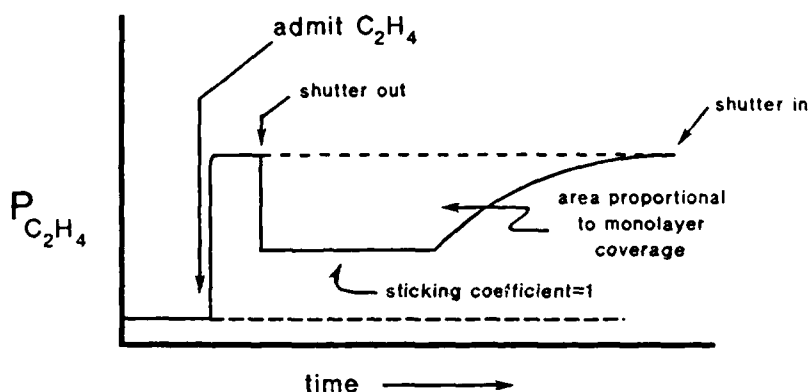


Figure 2. Apparatus for Kinetic Studies of Adsorption on Si(100)- Schematic Experimental Results.

Given that the sticking coefficient is initially unity, it is possible to determine the fraction of the flux of C_2H_4 which intercepts the crystal, using the fractional initial decrease in $P_{C_2H_4}$ upon opening the shutter. In our case, for a doser-to-crystal distance of 1.0 cm, the fractional interception is $.61 \pm .03$. This agrees well with the value determined from calculations of the doser performance using the known geometrical arrangement (crystal diameter = 1.6 cm; capillary array doser diameter = 1.06 cm), where a fractional interception value of $0.52 \pm .05$ is calculated [9].

IV. EXPERIMENTAL RESULTS

A. Absolute Coverage of C_2H_4 on Si(100)

A number of measurements have been made of the saturation coverage of C_2H_4 on Si(100). These are listed below in Table I.

Table I

Saturation Coverage of C_2H_4 on Si(100)
 (Crystal Area = 1.96 cm^2)
 Crystal T = 105 K.

Experiment No.	Adsorbate	Number of Molecules Incident (10^{14} cm^{-2})	Number of Molecules Adsorbed (10^{14} cm^{-2})	Saturation Coverage, C_2H_4 /dimer
1. 472	C_2H_4	3.9	1.21	.36
2. 485	C_2H_4	2.5	1.14	.33
3. 491	C_2H_4	2.9	1.27	.37
4. 492	C_2H_4	2.8	1.20	.35
5. 581	C_2H_4	2.9	1.29	.38
6. 622	C_2H_4	2.4	1.20	.35
7. 623	C_2H_4	2.8	1.21	.36
8. 641	C_2H_4	2.8	1.28	.38
9. 651	C_2H_4	2.2	1.04	.30
10. 653	C_2H_4	2.2	1.04	.31
11. 661	C_2H_4	2.3	.94	.28
12. 772	C_2D_4	2.3	1.09	.32
13. 685	C_2D_4	4.1	1.35	.40
14. 687	C_2D_4	4.3	1.07	.31
15. 692	C_2D_4	4.3	1.11	.33
16. 695	C_2D_4	4.3	1.10	.32
17. 775	C_2D_4	4.0	1.14	.33

Average = 0.34 ± 0.03
 C_2H_4 /Si dimer

B. Adsorption of C_2H_4 via a Precursor State Mechanism

The initial sticking coefficient of unity persists until a fraction of a monolayer of chemisorbed ethylene has been adsorbed, as indicated by the initial flat region in the schematic experimental curve shown in Figure 2. This may be understood from Figure 3, where, in the right hand side of the figure, C_2H_4 migrates over filled Si sites until an empty chemisorption site is found and occupied. Adsorption via a mobile precursor state is well known in adsorption studies on metals and has been recently reviewed [10]. In the left hand side of Figure 3, a schematic potential energy diagram is shown in which adsorption into the precursor state is followed by two possible kinetic processes: (1) desorption from the precursor with rate constant k_d ; and (2) chemisorption onto an empty site with rate constant k_r .

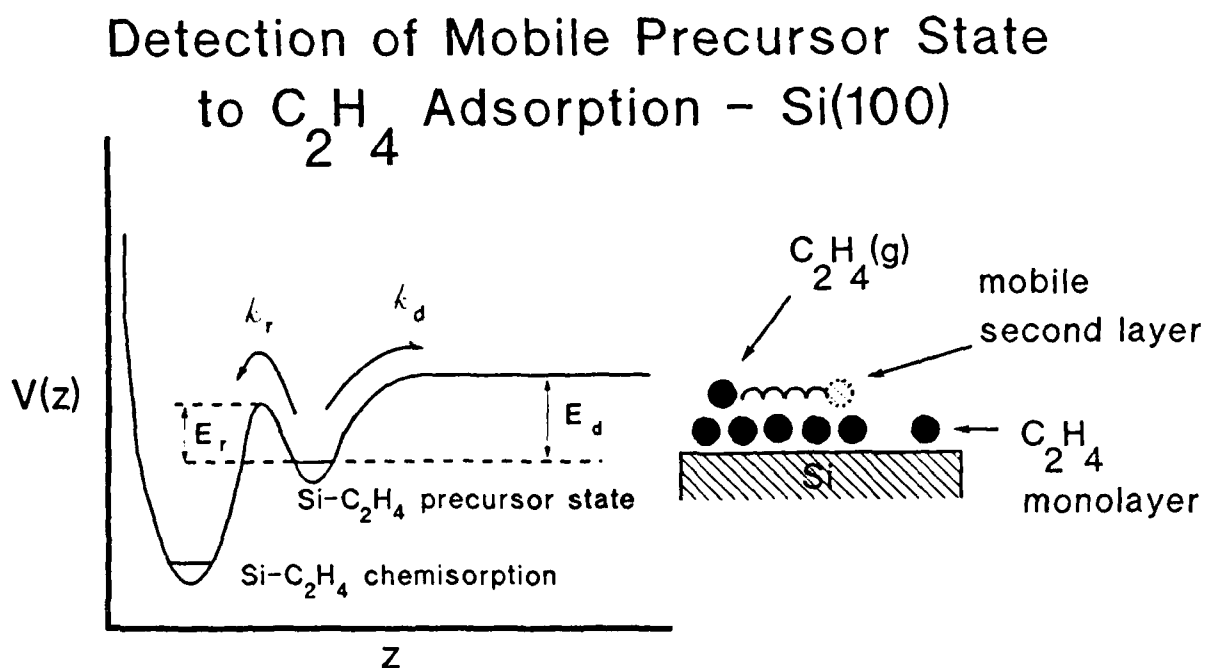


Figure 3. Mobile Precursor State to C_2H_4 Adsorption on Si(100).

Modeling this process, we obtain the relations:

$$P_{ad} = \frac{F}{1 + \frac{k_d}{k_r(1-\theta_r)}} \quad (1)$$

where P_{ad} = probability of adsorption

F = flux of molecules to the crystal

k_d, k_r = rate constants for desorption and reaction

θ_r = fraction of a chemisorbed monolayer

$$\frac{k_d}{k_r} = \frac{v_d}{v_r} e^{-\frac{E_d-E_r}{kT}} \quad (2)$$

where v_r, v_d = pre-exponential factors, and E_r, E_d = energy barrier to reaction or desorption.

From these equations, it is clear that we can find the energy difference between reaction and desorption, (E_d-E_r) and the ratio of the pre-exponential factors (v_d/v_r) by characterizing the different probabilities of adsorption with varying crystal temperature.

The rates of the two processes will vary differently with temperature as may be seen from the different activation energies for desorption and reaction from the precursor, and this fact may be used, as shown in equation 2, to determine the value of $(E_d - E_r)$. In our experiments we have used a temperature range from 103 K to 405 K and have studied the influence of temperature on the initial rate of adsorption by the clean crystal. Representative data are given in the top of figure 4 for the various temperatures; an Arrhenius plot yields $(E_d - E_r) = 2.9$ kcal/mole, and $v_d/v_r = 27$.

C_2H_4 / Si(100) - Rate of Adsorption versus Temperature

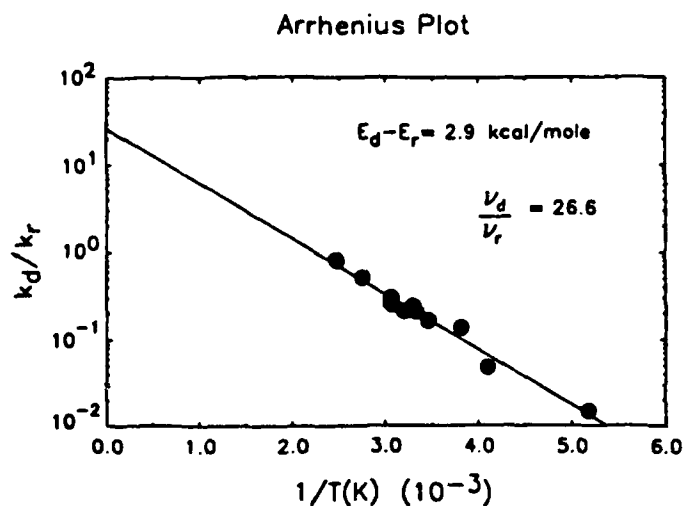
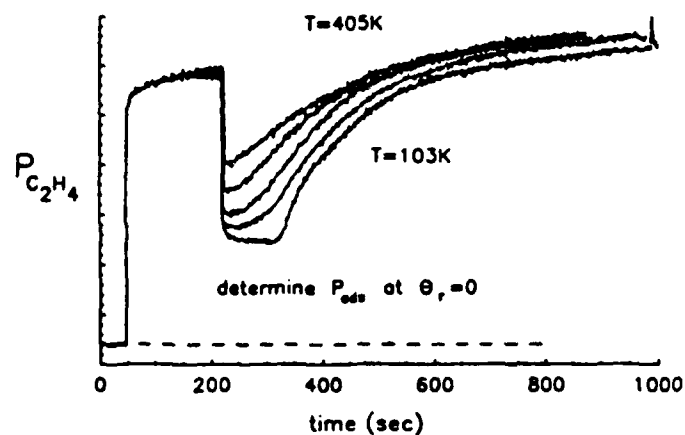


Figure 4. C_2H_4 Adsorption Kinetics on Si(100).

If we accept as a first approximation that E_d is equal to the heat of vaporization of $C_2H_4 = 3.5$ kcal/mole [11], then $E_r = 0.6$ kcal/mole. To the extent that E_d is greater than its heat of vaporization because of additional binding in the second layer, then E_r will also increase.

Within the confines of the transition state theory, the ratio of preexponential factors has physical meaning. Thus, the entropy of activation for desorption from the mobile precursor is greater than the entropy of activation for reaction. This implies that the transition complex for reaction is of lower entropy than the transition complex for desorption, that is, the reaction with the adsorption site involves a transition complex which is constrained entropically compared to the transition complex involved in desorption from the mobile precursor.

C. Desorption of C_2H_4 from Si(100).

Desorption experiments were carried out using both ethylene and deuterated ethylene (C_2D_4). A survey of all desorbing gases in the mass range 2, 4, 12 - 64 amu revealed that only ethylene and hydrogen desorbed from the surface in the temperature range 100 - 1000 K. Only a single desorption feature is observed for ethylene as shown in figure 5, where a sharp desorption peak with increasing peak temperature in the range 554 K to 591 K is observed, as the initial coverage is increased. The desorption kinetics, assuming first order desorption, was fitted according to the method of Chan et al [12], giving E_d (from the chemisorbed state) = 38.0 kcal/mole (figure 6), and $\nu_d = 10^{13.7} \text{ sec}^{-1}$, in the limit of zero coverage.

THERMAL DESORPTION OF ETHYLENE FROM SILICON(100)

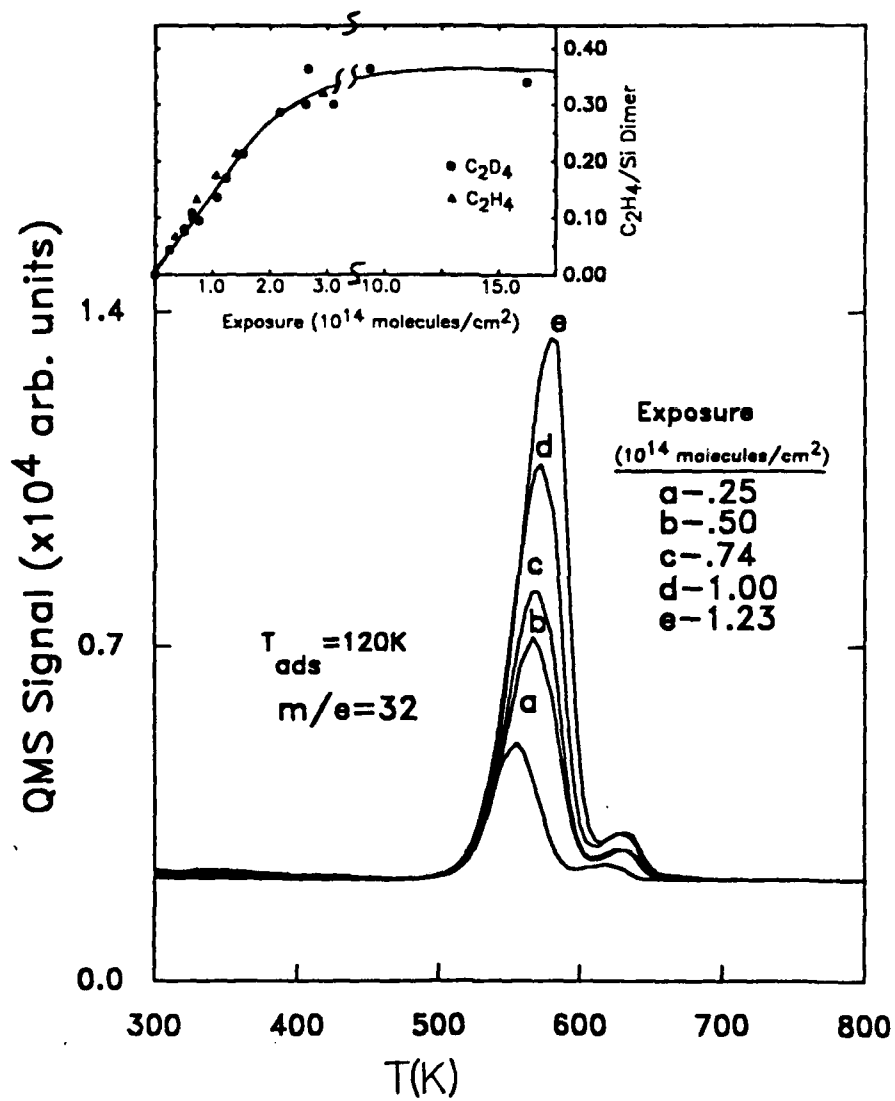
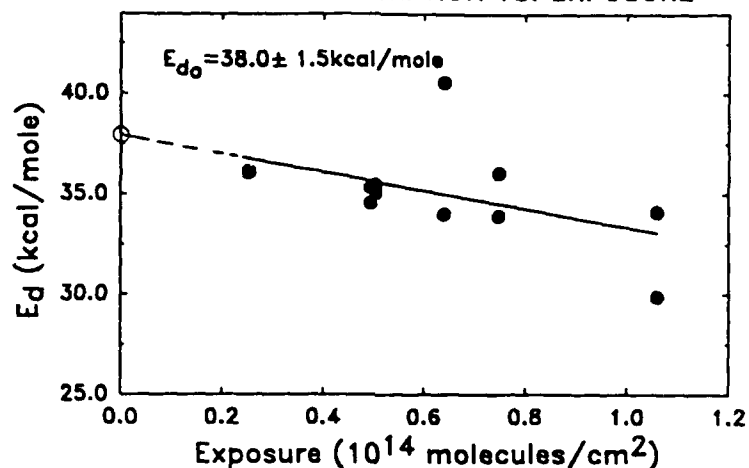


Figure 5. Thermal Desorption of C₂H₄ from Si(100).

ETHYLENE ON SILICON(100)

ENERGY OF DESORPTION VS. EXPOSURE



PRE-EXPONENTIAL FACTOR VS. EXPOSURE

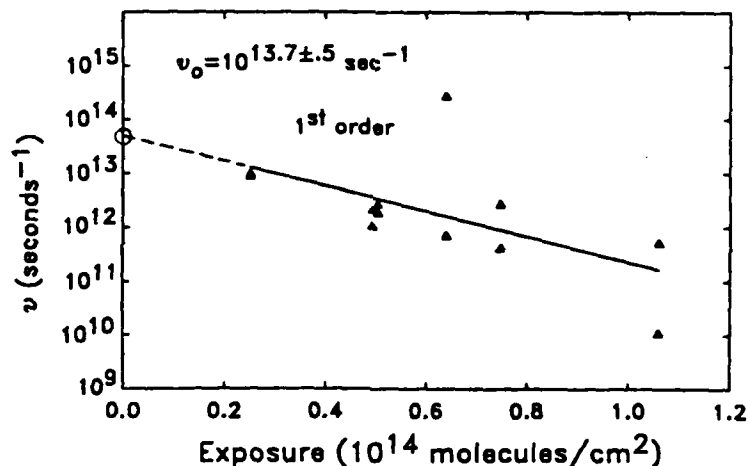


Figure 6. Desorption Rate Parameters- $\text{C}_2\text{H}_4/\text{Si}(100)$.

D. Decomposition of C_2H_4 on $\text{Si}(100)$.

It is well known that C_2H_4 will inefficiently decompose on $\text{Si}(100)$ at elevated temperatures. Thus, in the work of Bozso et al [13], an efficiency of about 10^{-3} SiC units per C_2H_4 collision with $\text{Si}(100)$ at 940 K was measured. Subsequent work by Taylor, et al [14] remeasured this efficiency, finding an efficiency of about 10^{-4} - 10^{-5} SiC units per C_2H_4 collision at 970 K. We have shown that chemisorbed C_2D_4 also inefficiently decomposes upon heating a monolayer above the desorption temperature, as shown in figure 7. Here, the thermal desorption of C_2D_4 was interrupted at various temperatures and the remaining carbon was measured by Auger spectroscopy. It may be seen that near 600 K the carbon surface concentration drops to near zero as C_2D_4 desorption is completed. Auxillary experiments, in which the amount of desorbing deuterium is measured following C_2D_4 desorption, have shown that less than about 4% of the C_2D_4 is decomposed on heating. Such low levels of reactivity could well be attributed to the presence of surface defects on the $\text{Si}(100)$ crystal.

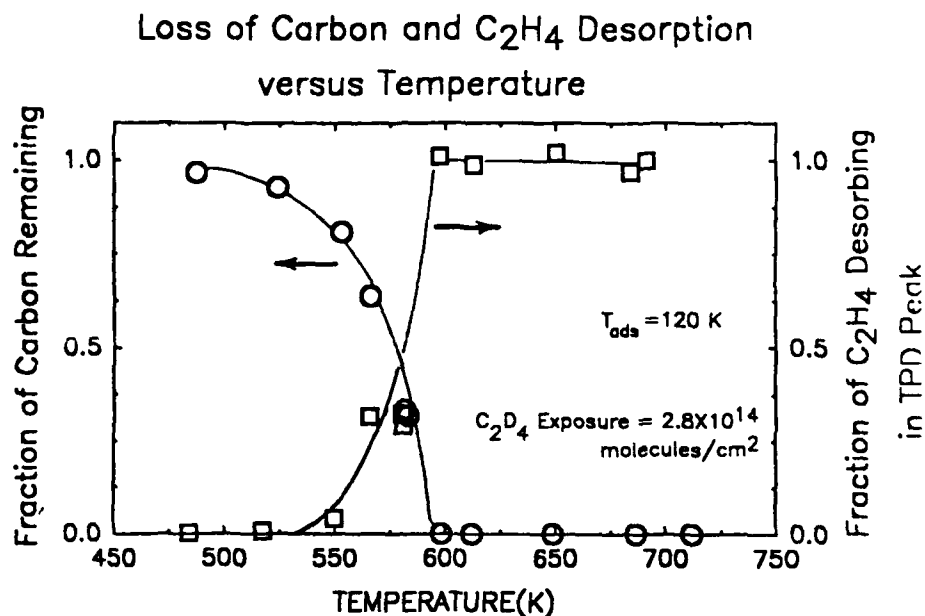


Figure 7. Loss of Carbon and C₂D₄ Desorption versus Temperature.

V. SUMMARY

The following accomplishments have been made in the past year.

1. An apparatus for quantitative studies of the kinetics of adsorption and the stoichiometry of adsorption has been constructed.
2. The adsorption of ethylene by Si(100) has been studied. It has been found that the adsorption process occurs via the involvement of a mobile precursor state which initially causes the ethylene sticking coefficient to be unity at temperatures near 100 K.
3. The kinetics of desorption and reaction from the mobile precursor have been studied, and the difference in activation energy for desorption and for reaction, ($E_d - E_r$) has been measured to be 2.9 kcal/mole.

4. The kinetics of desorption of ethylene from its chemisorbed state has been measured, yielding $E_d = 38.0$ kcal/mole and $v_d = 10^{13.7} \text{ sec}^{-1}$ for first order kinetics.
5. Nearly 100% of the chemisorbed ethylene desorbs from Si(100) with little decomposition to surface carbon occurring.
6. The saturation coverage of ethylene is estimated to be $0.34 \text{ C}_2\text{H}_4/\text{Si dimer}$. Surface models consistent with this measurement are being developed.

VI. REFERENCES

1. M. J. Bozack, P. A. Taylor, W. J. Choyke, J. T. Yates, Jr., *Surface Science* 179 (1987) 132.
2. J. Yoshinobu, H. Tsuda, M. Onchi, M. Nishijima, *J. Chem. Phys.* 87 (1987) 7332.
3. M. J. Bozack, P. A. Taylor, W. J. Choyke, J. T. Yates, Jr., *Surface Science* 177 (1986) L933.
4. D. Haneman, *Rep. Prog. Phys.* 50 (1987) 1045.
5. M. A. Van Hove, et al Low Energy Electron Diffraction, Springer-Verlag, Berlin, 1986, p. 274.
6. M. J. Bozack, L. Muehlhoff, J. N. Russell, Jr., W. J. Choyke, J. T. Yates, Jr., *J. Vac. Sci. Technol.* A5 (1987) 1.
7. M. J. Bozack, W. J. Choyke, L. Muehlhoff, J. T. Yates, Jr., *J. Appl. Phys.* 60 (1986) 3750.
8. R. J. Hamers, R. M. Tromp, J. E. Demuth, *Phys. Rev. B* 34 (1986) 5343.
9. A. Winkler, J. T. Yates, Jr., *J. Vac. Sci. Technol.* A6 (1988) 2929; C. T. Campbell and S. M. Valone, *ibid*, 13 (1985) 408.
10. W. H. Weinberg, H. J. Kreuzer, and M. Grunze in Kinetics of Interface Reactions, Springer-Verlag, Berlin, 1987, p. 94.
11. CRC Handbook of Chemistry and Physics, 63rd edition, R. C. Weast and M. J. Astle, eds., CRC Press, Inc., Florida, 1982, p. C-727.
12. C. M. Chan, R. Aris, W. H. Weinberg, *Appl. Surf. Sci.* 1 (1978) 360.

13. F. Bozso, J. T. Yates, Jr., W. J. Choyke, L. Muehlhoff, J. Appl. Phys. 57 (1985) 2771.
14. P. A. Taylor, M. Bozack, W. J. Choyke, J. T. Yates, Jr., J. Appl. Phys., submitted.

APPENDIX IV

CATHODOLUMINESCENCE EXPERIMENTS

I. Description of the Apparatus

A schematic of the apparatus is shown in side view in Figure 1. It consists of an electron gun for excitation of the emission, UHV sample chamber, and optics to spectroscopically analyze the cathodoluminescence emission.

Ultrahigh vacuum techniques are necessary to make sure that there are no condensed films on the sample. The electron gun energies were selected to excite samples as thin as tens of angstroms, and almost all gases from leaks, desorption, or backstreaming would condense on the samples that are maintained at cryogenic temperatures. Particularly, carbonaceous pump oils irradiated by the electron beam would be expected to appear very "diamond-like." The only way to avoid surface contamination is to make sure that monolayer formation times are longer than experiment times. The turbo-backed ion pump and sorption pumps used in the sample chamber maintain pressures of 5×10^{-11} torr. The cryogenic sample heat shields maintain pressure at the sample at 10^{-11} to 10^{-12} torr, depending on temperature of operation. The turbo is also used to back the rotating seal on the sample turret, which will be discussed later.

The monochromator is a custom-made 1 meter Ebert vacuum instrument. Fused silica and sapphire optics permit operation at wavelengths down to the cutoff in air at about 1850 in the present configuration, but it is possible to vacuum-couple the instrument to the sample chamber if required. The optical arrangement contains a beam splitter which superimposes a wavelength calibration line spectrum, e.g., mercury, on the measured spectrum.

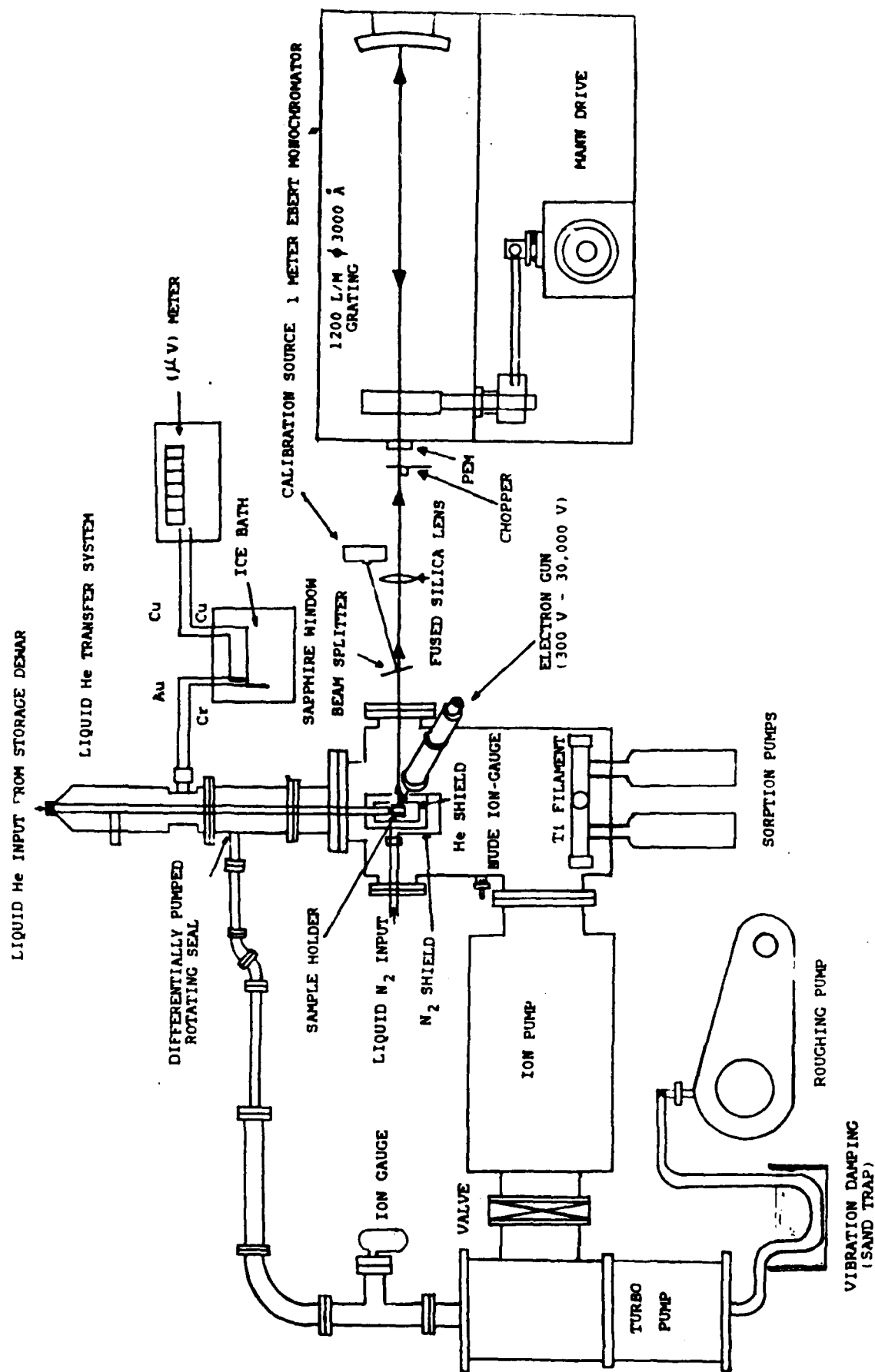


Figure 1. Schematic of the cathodoluminescence experiment (side view).

The details of the six-position, rotatable sample turret are shown in Figure 2. One of the six sample positions is occupied by a phosphor which is used for alignment by positioning a laser to coincide with the electron beam-excited spot. This spot is focussed on the monochromator entrance slit, so when samples are rotated into the laser spot they are automatically in the correct position both for the electron beam and for the analyzing optics. The electron beam energy can be varied from 300V to 30 kV, corresponding to a wide range of stopping distances in the materials of interest here.

Three samples of cathodoluminescence spectra measured with this apparatus are presented below. Figure 3 shows the spectrum from a natural type IIb diamond, giving a broad band in the blue with few features. The sharp lines are the superimposed calibration lines, and the computerized data management routine interpolates between these lines to determine the wavelength scale. The spectrum shown in Figure 4 was taken at room temperature on a synthetic polycrystalline diamond film deposited at Westinghouse R&D Center, and the spectrum in Figure 5 of this same sample taken at 60K shows a shift of the main band toward higher energies, as would normally be expected.

We are currently analyzing these data to identify the bands and features of the spectra. Also, a variety of samples prepared under tightly characterized conditions is being obtained in order to study the influence of dopants and defects, and to provide a baseline of knowledge for studying the materials that are produced on this program.

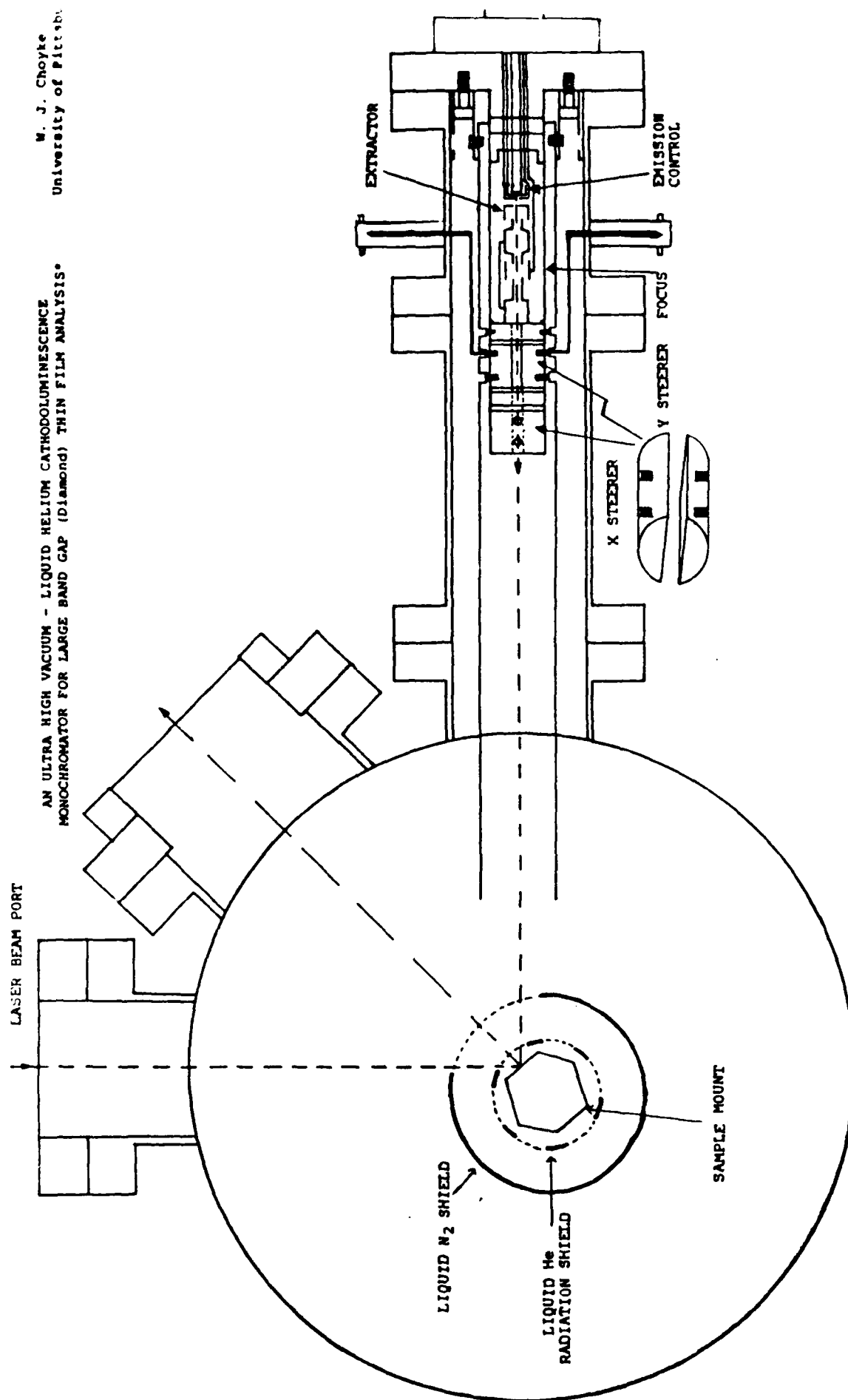


Figure 2. Detail of the sample turret, electron gun, and the optical alignment and monochromator arrangements.

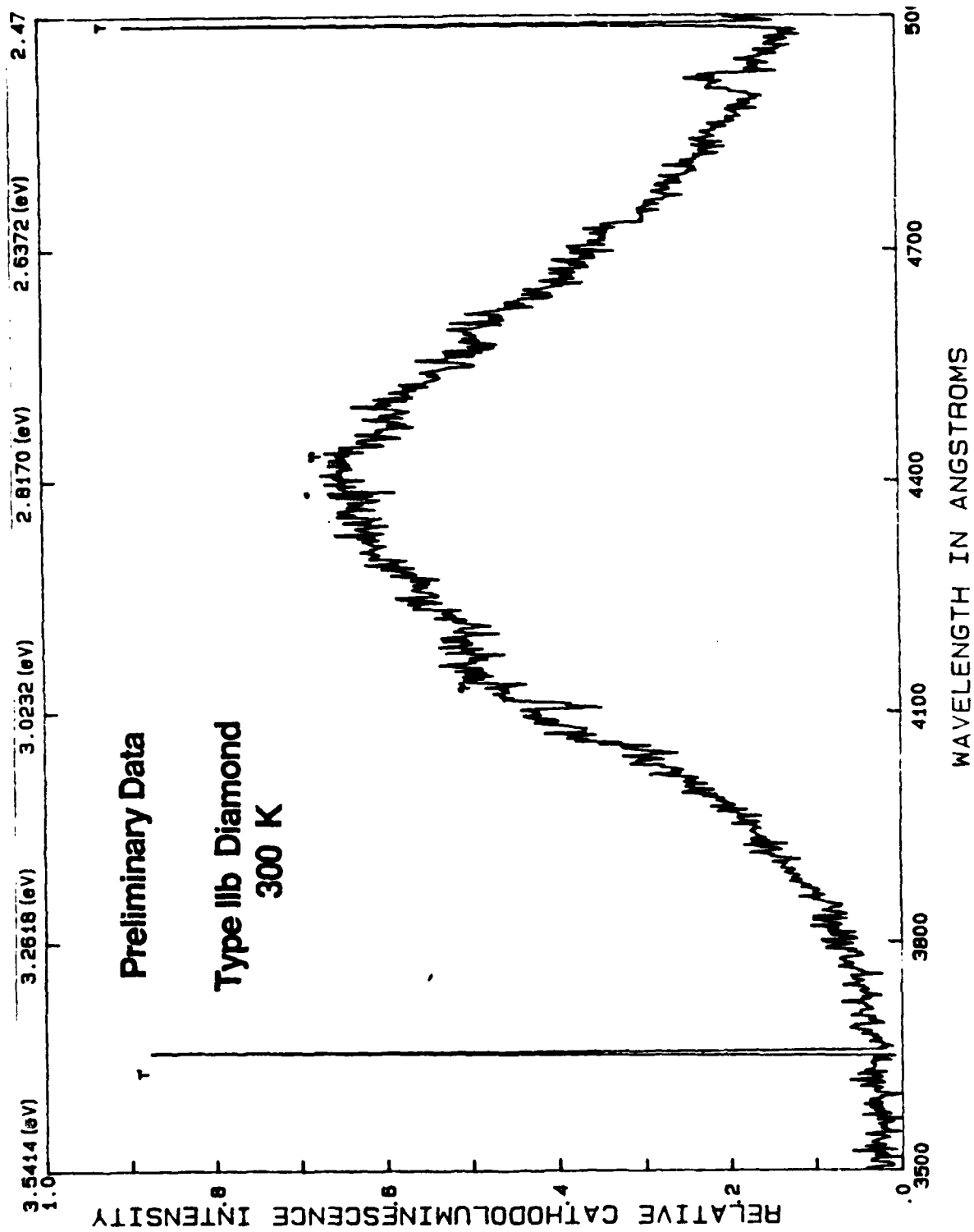


Figure 3. Cathodoluminescence spectrum of type IIb diamond at 300K.

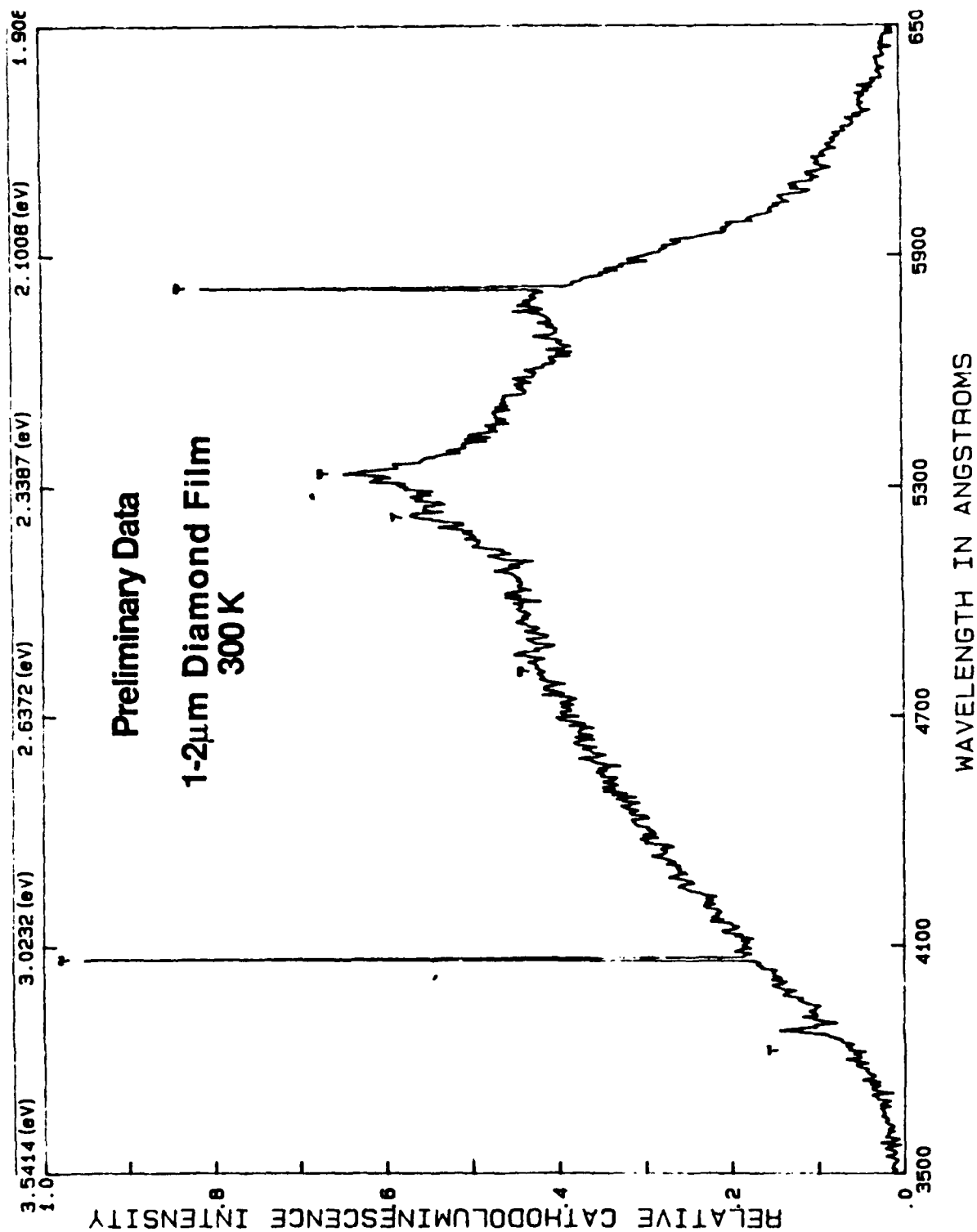


Figure 4. Cathodoluminescence spectrum of a polycrystalline diamond film at 300K.

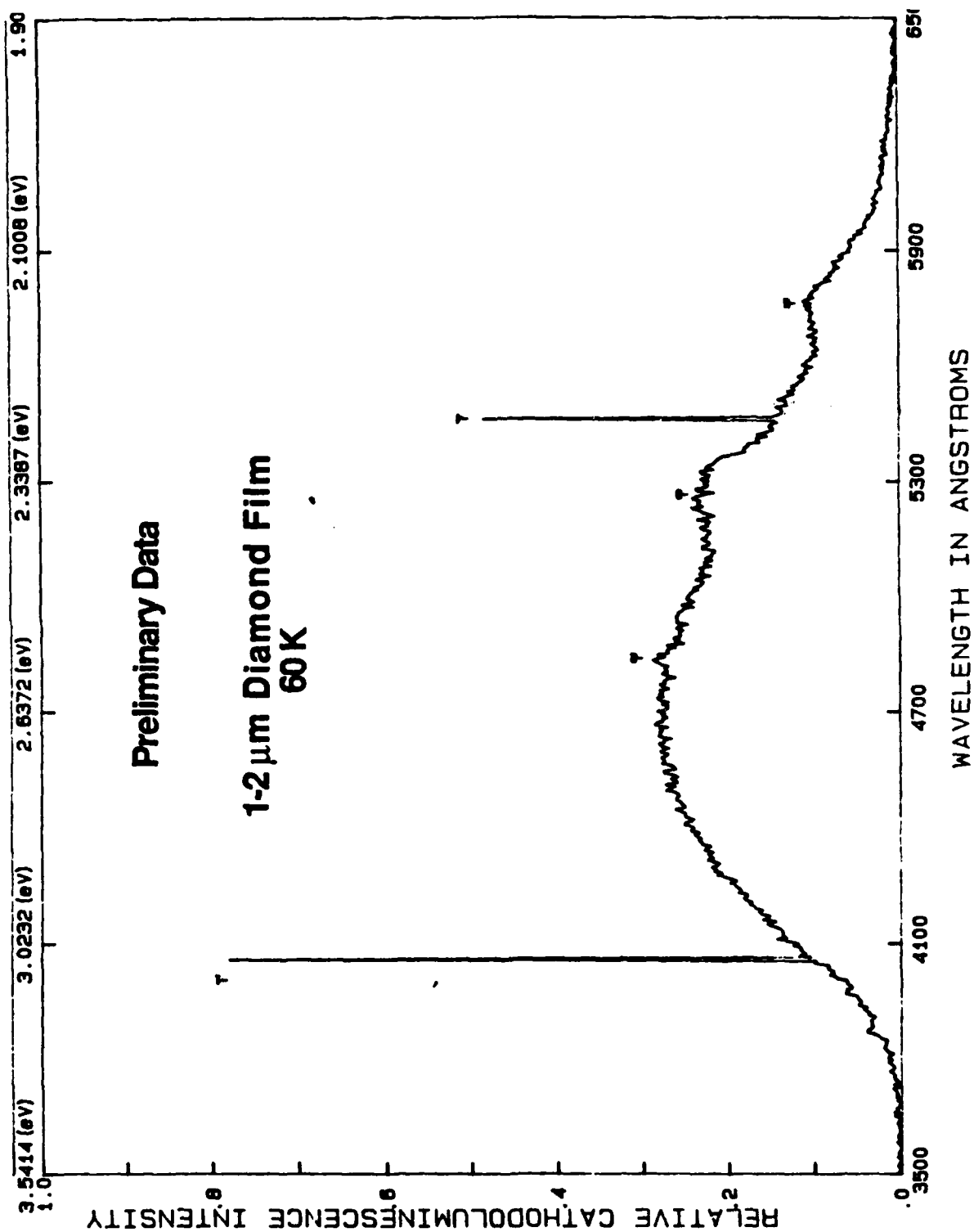


Figure 5. Cathodoluminescence spectrum of a polycrystalline diamond film at 60K.